# Covalent Functionalization of Two-Dimensional Group 14 Graphane Analogues

| | |
|---|---|
| Journal: | *Chemical Society Reviews* |
| Manuscript ID | CS-REV-04-2018-000291.R1 |
| Article Type: | Review Article |
| Date Submitted by the Author: | 29-May-2018 |
| Complete List of Authors: | Huey, Warren; The Ohio State University, Chemistry and Biochemistry<br>Goldberger, Joshua; The Ohio State University, Chemistry and Biochemistry |
| | |

Chem Soc Rev

Review Article

# Covalent Functionalization of Two-Dimensional Group 14 Graphane Analogues

Warren L. B. Huey[a] and Joshua E. Goldberger*[a]

Received 00thJanuary 20xx,
Accepted 00th January 20xx

DOI: 10.1039/x0xx00000x

**www.rsc.org/**

The $sp^3$-hybridized group 14 graphane analogues are a unique family of 2D materials in which every atom requires a terminal ligand for stability. Consequently, the optical, electronic, and thermal properties of these materials can be manipulated via covalent chemistry. Herein, we review the methodologies for preparing these materials, and compare their functionalization densities to Si/Ge(111) surfaces and other covalently terminated 2D materials. We discuss how the electronic structure, optical properties, and thermal stability of the 2D framework can be broadly tuned with the ligand identity and framework element. We highlight their recent application in electronics, optoelectronics, photocatalysis, and batteries. Overall, these materials are an intriguing regime in materials design in which both surface functionalization and solid-state chemistry can be uniquely exploited to systematically design properties and phenomena.

## A. Introduction

Two-dimensional (2D) materials have become one of the most well studied families of compounds over the last 15 years. Graphene's discovery has shown that it is not only possible to extract, isolate, and study the properties of single atom thick layers from 2D van der Waals materials, but that these materials can have completely different properties compared to the unexfoliated bulk structure.[1] The band gap, its direct or indirect nature,[2] the chemical reactivity,[3] the magnetic behavior,[4] and the thermal properties[5] can have a pronounced layer dependence.[6] Also, there has been considerable interest in new phenomena that emerge with the unique electronic structures arising in the few-layer regime. For instance, there has been considerable interest in creating 2D topological insulator materials that exhibit quantum spin Hall and quantum anomalous Hall states, on account of their perfect, dissipationless edge channel conductivities. Furthermore, these materials have been explored in many different applications ranging from electronics (i.e. field effect transistors, photovoltaics, sensing) to membrane technologies (i.e. desalination, nanopore sensing) to energy storage and catalysis (i.e. supercapacitors, photocatalysis, water-splitting).

One consequence of designing materials with atomic-scale thicknesses is that their relevant properties are extremely sensitive to their local surroundings. The covalent functionalization of 2D materials is one way to both interface these ultrathin materials with the outside world and manipulate their inherent properties. For instance, covalent functionalization can tune the internal bond lengths and bond angles of the 2D material framework and thus change its electronic structure. In addition, the local dielectric constant, the hydrophobicity, and the thermal stability can be controlled by grafting different ligands.

The Si, Ge, and Sn analogues of graphene require ligand termination on every atom to be stable under ambient conditions, and therefore are ideal 2D systems for understanding the influence of surface functionalization. Graphene consists of carbon atoms arranged in a honeycomb network, where each carbon atom has 3σ and 1π bond with its three nearest neighbors. In the Si, Ge, and Sn derivatives of graphene, the σ bond distances are much larger with significantly reduced π-orbital overlap, and as a consequence these analogues would have much weaker π-bonds. As a result, there is a strong thermodynamic preference for these materials to have a fourth σ bond to a terminating ligand. In other words, the group 14 graphane materials are stabilized via surface functionalization. Using the parlance of organic chemistry in which molecules with double bonds end in "-ene", and molecules with single bonds end in "-ane", we define these ligand terminated group 14 analogues as "silicane", "germanane", or "stanane".

Herein, we review the surface functionalization chemistry of group 14 graphane analogues, in comparison to Si/Ge(111) surfaces as well as other 2D materials. Before discussing specific surface functionalization reactions, we will first establish the various parameters that are important to quantify when comparing different chemical routes. We will highlight methods to prepare hydrogen and organic-terminated group 14 graphane materials starting from the direct topotactic transformation of Zintl phases. Then we will describe the established chemical methodologies for directly substituting one surface ligand with another. These will be compared with methods that have been developed for other

---

[a] Department of Chemistry and Biochemistry, The Ohio State University, Columbus, OH 43210, USA
E-mail: goldberger.4@osu.edu

2D material systems including graphene, transition metal dichalcogenides, and the phosphorene derivatives. Then, we will establish how the electronic and thermal properties of these materials can be manipulated via the identity of the ligand. Finally, we will highlight the different applications in which these functionalized 2D materials have been used.

## B. Surface Functionalization Metrology

Before discussing the various chemical methods to prepare surface functionalized 2D materials, it is important to establish guidelines for comparing the effectiveness of each route. For each functionalization reaction numerous questions must be addressed such as; what new ligand or mixtures of ligands are on the surface? If there are mixtures of ligands what is their relative ratio? How are they bonded to the framework? Are they polymerized on top of the framework? Does functionalization change the structure or amorphize the 2D material? What are the thermal and chemical stabilities of the product? If the scope of a functionalization method is sufficiently broad enough to derivatize these frameworks and bond with different ligand types, are there systematic changes in stability and properties?

Answering these questions requires significant experimental effort. It is straightforward to identify the existence of a functional group bonded to the surface of a 2D material via Fourier Transform Infrared Spectroscopy (FTIR), Raman spectroscopy, and Scanning Tunnelling Microscopy (STM). However, Raman and FTIR do not provide quantitative insight to the degree of ligand substitution. In our experience, the combination of C:H:M (M = metal) elemental analysis and thermogravimetric analysis (TGA) can give estimates of the ligand functionalization density within 5%, but it can be difficult to quantify O-containing species. X-ray Photoelectron Spectroscopy (XPS) can be used, but is often convoluted by the presence of adventitiously adsorbed C- and O-containing species from the environment, and it cannot detect H. Synchrotron X-ray diffraction experiments and pair-distribution function (PDF) measurements can give rough estimates of the degree of amorphization. We have observed that the material properties such as the optical absorption are more sensitive to the presence of amorphization. In germanane (GeH), the absorption onset can shift to lower energies once a small percentage of the 2D material starts to amorphize. In total, probing the functionalization of these 2D materials can be very complicated, and require the combination of all of these methods and sufficient quantities of material. Still, to advance our understanding, it is essential that researchers rigorously and systematically quantify all aspects of the composition, structure, crystallinity, and their effects on the properties of these materials.

## C. Functionalization of (Si/Ge) (111) Surfaces by Analogy

Before discussing the functionalization of the 2D group 14 graphane materials, it is worthwhile to first review the different methods that have been established to functionalize the Si/Ge(111) surfaces due to their structural similarity. These materials crystallize into the diamond structure type, and have (111) surfaces that are isostructural to these group 14 graphane analogues (**Fig. 1**). These (111) surfaces consist of a puckered, honeycomb arrangement of group 14 atoms, so that every other atom is coordinatively unsaturated, and thus can be terminated by a ligand. Typically, Si/Ge often feature an amorphous oxide layer that must be removed before further functionalization can occur. For instance, it is well established that the native $SiO_2$ layer on Si wafers can be stripped off via HF rinsing, leaving a Si–H surface that is stable in air for a limited period of time (**Fig. 2a**). The native $GeO_2$ surface is much less stable and is readily washed away in water or acid.

Thus far, three major methodologies have been established to functionalize Si/Ge(111) surfaces, including Grignard chemistry, hydrosilylation and hydrogermylation, and electrochemical grafting methods.[7, 8] First, the Grignard approach involves forming Si/Ge-halogen bonds on the (111) surface (**Fig. 2b**), which subsequently react with Grignard reagents (i.e. $CH_3MgBr$) to form M–R bonds (**Fig. 2c**).[9] For instance, the formation of Ge(111)–$CH_2CH_3$, initially reported in 1962, was accomplished via the formation of electrophilic Ge–Cl surfaces by reacting Ge(111) with HCl and $Cl_2$ gasses, which are subsequently reacted with the nucleophilic $CH_3CH_2MgBr$.[10] Over the past few decades, this chemistry has been expanded significantly to create and study the properties of a wide variety of organic terminated Si/Ge(111)–R surfaces (**Table 1**).

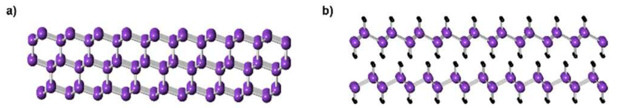

**Fig. 1** a) Atomic structure of Germanium (111) surface, and b) the 2D germanane framework, highlighting their structural similarities. Germanium atoms are purple, and hydrogen atoms are black.

The second approach to functionalize these surfaces involves the insertion of alkenes and alkynes into Si(111)–H surfaces, which is referred to as hydrosilylation (**Fig. 2d**).[7, 8, 11, 12] Oftentimes this reaction requires a radical initiator to first strip off a proton of the Si(111)–H surface leaving behind a Si surface radical. This radical then bonds with the alkene or alkyne, producing a radical on the β-carbon, which then abstracts a proton from a nearby Si(111)–H bond. This process continues to propagate until free radical termination. Similarly, Si(111)–H scission can be initiated photochemically, to produce the radical surface. Instead of going through a free-radical mechanism, hydrosilylation can be achieved catalytically using either Lewis acid catalysts, or late transition metal catalysts, including Pt/Pd-based ones. These catalytic cycles involve insertion of the catalyst into the Si–H bond either along with the addition of the alkene or alkyne onto the metal center. The Si–R group is formed via elimination from the catalyst. While the analogous hydrogermylation of Ge(100)–H surfaces has been established,[13] surprisingly, to the best of our knowledge, there are no reports to date showing this can be extended to Ge(111)–H surfaces.

The final method to form Si/Ge(111)–R is electrochemical based functionalization, which utilizes silicon or germanium substrates as electrodes (**Fig. 2e,f**). In most proposed cathodic mechanisms, either the Si/Ge–H bonds or the ligand are reduced electrochemically using a one-electron process.[14] In the latter case, the ligand radical then reacts with Si/Ge(111)–H to generate a radical Si/Ge(111) on the surface, which subsequently reacts with a second ligand radical to form a covalent bond. For instance cathodic grafting of Si(111) surfaces with 4-bromo or 4-nitro aryl diazonium salts has been shown to proceed via this mechanism, and has produced phenyl-terminated surfaces.[15] In the anodic functionalization process (**Fig. 2d**) the Si/Ge–H is first electrochemically oxidized by one electron to form the radical cation, enabling the insertion of an alkyne or alkene into this bond. The grafted product, which is still a radical cation, oxidizes a neighboring Si/Ge–H again forming a radical cation. For an alkyne, these neighbors then combine to form a bridging alkane radical cation. This bridging alkane then oxidizes its neighboring Si/Ge–H allowing the propagation of the reaction to occur. For alkenes, once grafted they oxidize their neighbor allowing the propagation to occur but do not bridge between neighbors. As a consequence of the mechanism, anodic grafting produces fully saturated organic ligands lacking double bonds.

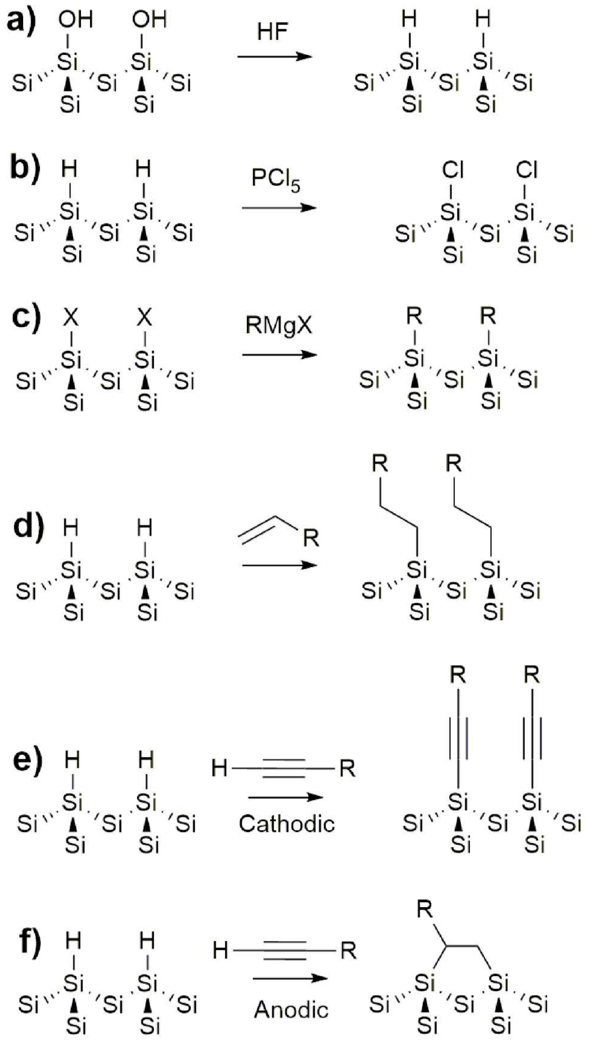

**Fig. 2.** Methodologies for generating a) Si(111)-H and b) Si(111)-Cl surfaces. Products of Si/Ge(111)-R functionalization using c) Grignard reagents, d) Hydrosilylation or Hydrogermylation with a free-radical mechanism, and e) cathodic, and f) anodic electrochemical grafting.

More recently, a variety of methodologies have been developed to graft Si/Ge(111) surfaces with group 14-16 linkages via reacting with organoamines and hydrazines. First, halogenated Si(111) surfaces can react directly with ammonia, amines, hydrazine, or organohydrazine groups, in a dehydrohalogenation process. Indeed, the formation of C- and O- free Si(111)-$NH_2$ has been observed via the reaction of Si(111)-Cl with $NH_3$ in THF.[16] Also, the formation of Ge(111)-SR is readily achieved via the direct reaction of Ge(111)-Cl/Br with 1-alkane organothiols to form Ge(111)-SR.[17]

Surface science researchers have utilized these approaches to produce a multitude of ligand-terminated Si/Ge(111)-R surfaces. **Table 1** is a list showing some of the different ligand-functionalized surfaces that have been synthesized. In many cases, the combination of XPS, FTIR, and STM have confirmed the functionalization density of a Si(111).(**Fig. 3**) It is apparent that the sterics of the ligand can profoundly affect the density of functional groups that can be grafted. For instance only -halogen, -methyl, -acetylene, -propynyl, -ammonia, and -hydrazine can be grafted onto the surface such that every single Si- or Ge- atom is terminated with a functional group. However, even a small function group such as ethyl is too sterically bulky for complete termination on a Si(111) surface. The nearest neighbor distance between atop sites on a Si(111) surface is 3.84 Å and for Ge(111) is 4.00 Å. Atomistic models of ethyl-terminated Si(111) indicate that the closest distance between atoms on neighboring functional groups is between the H- atoms on the α-C, and the H-atoms on the β-C on a neighboring ethyl group, which can be <2.17 Å.[18] As a consequence, most organic substitutions are too large to fully terminate the surface. Still while density functional theory (DFT) predicts that steric restrictions imposed by the functional groups will limit the surface packing for $-CH_2CH_3$ to approximately 50% of surface sites, experimentally it has been shown via XPS that $-CH_2CH_3$ can be functionalized onto Si(111) at ~90 ± 20% of the surface sites relative to $-CH_3$.[19] This large value is due to the high density of step edges and edge pits that can form, as well as the exothermic nature of the covalent bond formation allowing for significant strain to occur. More recently, this limitation on functionalization has been overcome through the creation of surface functional groups having a mixture of -$CH_3$ and a much larger ligand.[20]

Ultimately, the inability to replace every Si/Ge(111)-H bond with a functional group severely limits the long term air- and water-stability of these surfaces.[9]

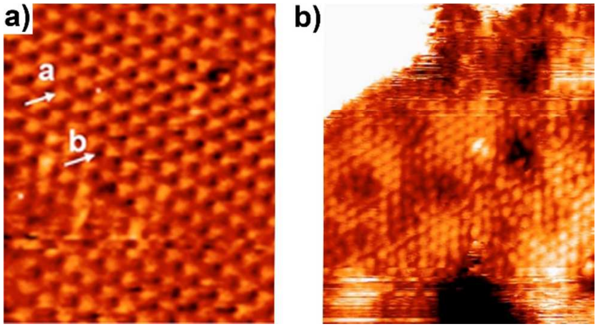

**Fig. 3**. STM images of a) Si(111)-$CH_3$ (Image size: 5x5 $nm^2$) acquired at −2 V and 0.3 nA and b) Si(111)-$C_2H_5$ (Image size: 10x10 $nm^2$) acquired at −3 V and 0.07 nA. Reproduced from ref. [18] with permission from Applied Physics Letters, copyright 2006.

## D. Synthesis of Graphane Analogues via Topotactic Transformation of Zintl Phases

The synthesis of group 14 graphane analogues is accomplished via the direct transformation of precursor intermetallic layered Zintl phases that possess the same single-atom thick puckered honeycomb structure as graphane. Zintl phases, or more precisely, phases that follow the Zintl-Klemm electron counting rules, refer to compounds comprised of the electropositive groups 1-3 and rare earth elements, combined with groups 13-16 *p*-block elements. The large electronegativity difference causes the electropositive elements to donate their valence electrons to the *p*-block elements. In their crystal structures, the *p*-block elements covalently bond with each other to form polyanion frameworks, to create a formal octet. For instance, the structure of the layered Zintl phases $CaSi_2$, $CaGe_2$, and $BaSn_2$ consist of layers of $Si^-$, $Ge^-$, and $Sn^-$ in a graphane arrangement separated by $Ca^{2+}$ or $Ba^{2+}$ cations (**Fig. 4a**). These materials react with electrophiles that bond with the Si/Ge/Sn framework to form covalently terminated SiR, GeR, and SnR.

### D.1 Topotactic transformation of $CaSi_2$

The very first report of the possible synthesis of these silicon graphane analogues was by Friedrich Wöhler in 1863. He reported the synthesis of hexagonal "graphite-like" platelets of $CaSi_2$ via the reaction of Na, $CaCl_2$, and Si powder. Upon treatment with different acids, they transformed into a yellow powder having an approximate stoichiometry of $Si_8O_4H_6$.[21] In the 1920's, Kautsky more precisely defined this material as having a stoichiometry of $Si_2H_2O$.[22] The structure of Kautsky's material, referred to as "siloxene", was originally proposed to consist of six-membered rings of Si that are separated from each other by Si-O-Si bridges, with each Si atom having a terminal hydrogen (**Fig. 4b**). This structural model was hypothesized from gas adsorption measurements.[23, 24] However, no such structure has ever been observed via X-ray diffraction experiments. In 1980, Weiss *et al.* collected X-ray structures of siloxene formed via reaction of $CaSi_2$ in aqueous HCl at room temperature and dried over $P_4O_{10}$.[25] Weiss proposed a structure of siloxene in which the honeycomb Si framework in $CaSi_2$ is terminated with –H and –OH substituents based on the change in lattice constants of siloxene (a=3.82 Å, c=6.33 Å/layer) from the 6-layer rhombohedral (6R) $CaSi_2$ (a=3.85 Å, c=5.10 Å/layer) (**Fig. 4c**). In 1962, Schott reported on his attempts to synthesize the pure hydrogen-terminated SiH graphane analogue, referred to as "layered polysilane" (**Fig. 4d**), using HCl/ethanol as well as a variety of other solvents, yet they always observed residual halogen and alkoxide formation.[26] In 1993, Dahn *et al.* reported that "layered polysilane" could be synthesized via the reaction of 6R $CaSi_2$ with aqueous HCl at 0 $^{o}$C under an inert $N_2$ atmosphere, filtered, rinsed in concentrated HF, and vacuum dried.[27] Compared to a siloxene sample that was prepared at 80 $^{o}$C (a=3.83 Å, c=5.90 Å/layer), the 0 $^{o}$C "layered polysilane" diffraction pattern was fit to a hexagonal structure with a much smaller *c*-axis lattice constant (a=3.83 Å, c=5.40 Å/layer) (**Fig. 5a**). FTIR is sensitive to the presence of Si-O vibrational modes, especially the extremely intense stretching mode at ~1000 $cm^{-1}$. In follow up work He *et al.,* showed that the FTIR spectra of layered polysilane prepared after -20 $^{o}$C HCl treatment and EtOH washing shows an Si-H stretch at 2100 $cm^{-1}$, an intense Si-O stretch at 1000 $cm^{-1}$, broad Si-O bending modes centered around 800 $cm^{-1}$, a broad O-H stretch from 3200-3600 $cm^{-1}$, and an O-H bending mode at 1620 $cm^{-1}$.[28, 29]

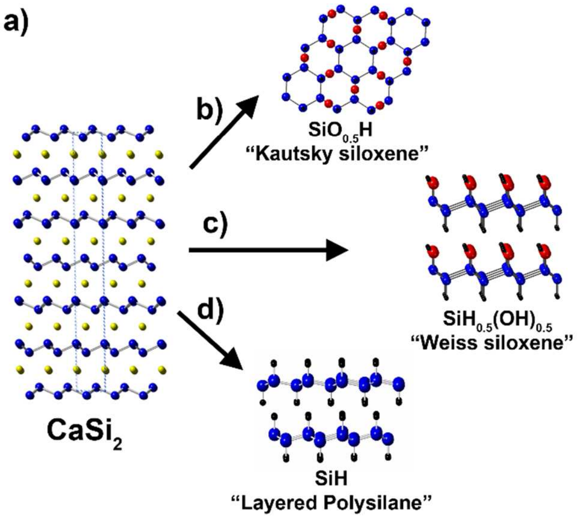

**Fig. 4.** a) Crystal structure of 6R $CaSi_2$. b) Kautsky's proposed structure of siloxene ($SiHO_{0.5}$) c) Weiss's proposed structure of siloxene. d) proposed structure of layered polysilane, or hydrogen-terminated silicane (SiH). Ca atoms are yellow, Si atoms are blue, H atoms are black, O atoms are red.

**Table 1.** Reported ligand terminated Si(111)-R and Ge(111)-R surfaces, with the measured ligand density, and synthetic method. MgR refers to Grignard approach, EG refers to electrochemical grafting, HS and HG refer to hydrosilylation or hydrogermylation, Dhh = Dehydrohalogenation, $PCl_5$ and $Br_2$ = halogenation, Quantitative determination of the Ligand Density was determined via XPS unless noted. †=Rutherford Backscattering, $^{\Pi}$= STM

| Ligand | Ligand Density | Synthesis Method | Ref. |
|---|---|---|---|
| ***Si(111)-R*** | | | |
| $-CH_3$ | 100(13)% | MgR | [9] |
| $-C{\equiv}CH$ | 63(8)% | Dhh | [30] |
| $-C{\equiv}CCH_3$ | 105(6)% | Dhh | [30] |
| $-OCH_3$ | 39(7)% | HS | [31] |
| $-CH_2\text{-}CH{=}CH_2$ | 80(5)% | MgR | [20,32] |
| $-(CH_2)_2C$(propylene glycolato) | -- | MgR | [33] |
| $-(CH_2)_2CHO$ | -- | MgR | [33] |
| $-CH_2CH_3$ | 85(13)% | MgR | [9,30,34] |
| $-(CH_2)_3CH_3$ | 68(3)% | MgR | [34] |
| $-(CH_2)_4CH_3$ | 76(8)% | MgR | [34] |
| $-(CH_2)_5CH_3$ | 60(1)% | MgR | [9, 34] |
| $-(CH_2)_7CH_3$ | 44(1)% | MgR, HS | [9,34,11] |
| $-(CH_2)_9CH_3$ | 36(6)% | MgR | [34] |
| $-(CH_2)_{11}CH_3$ | 42(5)% | MgR | [34] |
| $-(CH_2)_{15}CH_3$ | ~55% | HS | [12] |
| $-(CH_2)_{17}CH_3$ | 25(1)% | MgR, HS | [34,11,35,36] |
| $-Cl$ | ~99% | $PCl_5$ | [9,37] |
| $-Br$ | ~99%$^{\Pi}$ | $Br_2$ | [30,38] |
| $-C{\equiv}CC_6H_2F_3$ | 31(1)% | MgR | [39] |
| $-(CH_2)_2(CF_2)_5CF_3$ | ~27% | EG | [40] |
| $-C_6H_5$ | ~50% | EG | [41] |
| $-p\text{-}C_6H_4Br$ | ~47%† | EG | [42] |
| $-NH_2$ | 55(9)% | Dhh | [16] |
| $-NHNH_2$ | 107(8)% | Dhh | [37] |
| $-NHNH_2C_6H_5$ | 21(5)% | Dhh | [37] |
| $-NH(CH_2)_2NH-$ | 90(20)% | Dhh | [43] |
| ***Ge(111)-R*** | | | |
| $-Cl$ | 112(1)% | HCl | [10,17] |
| $-Br$ | 100(10)% | $Br_2$ | [44] |
| $-CH_3$ | 83(3)% | MgR | [45] |
| $-CH_2CH_3$ | -- | MgR | [10] |
| –alkanethiols | -- | Thiolation | [17] |

After HF treatment and multiple 0 °C MeOH washes, the FTIR spectra shows Si-H and Si-$H_2$ edge vibrations without any Si-O, Si-OH, or O-H modes (**Fig. 5b**). While these reports suggest that the direct transformation of $CaSi_2$ in HCl at low temperatures followed by careful HF treatment can indeed yield SiH instead of $SiH_{1-x}(OH)_x$, the extreme oxophilicity, insolubility, and reactivity of this intermediate complicates the acquistion of quantitative and conclusive evidence of oxygen-free materials. Indeed, in many published FTIR spectra of "SiH", Si-O bending and stretching modes are always apparent at ~840-870 $cm^{-1}$ and ~1000-1100 $cm^{-1}$, respectively.[46-48] The presence of these Si-O stretching modes in "SiH" starting materials will lead to questions about the exact functionalization chemistry of these materials.

Finally, the topotactic transformation of $CaSi_2$ was further explored via Bonitz in the 1960's, where he found that it can react with different $Cl_2$ sources ($PCl_5$, $SbCl_3$, $Cl_2$) in $CCl_4$ and $SiCl_4$, to oxidize the network and form an extremely reactive form of silicon which he called "active silicon".[49] This material would react with further equivalents of $Cl_2$ to form a material with the stoichiometry [SiCl], and then different perchlorinated molecular products, most notable of which are cyclic chlorosilanes (i.e. $Si_{10}Cl_{18}$, $Si_6Cl_{12}$). Likely due to its extreme reactivity, there have been no structural studies on "active silicon" to date.

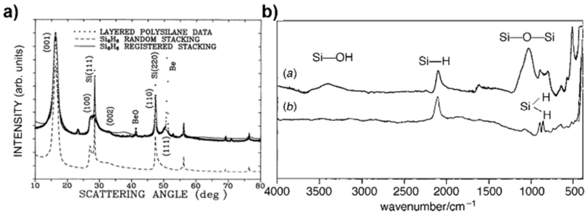

**Fig. 5.** a) The measured powder X-ray diffraction pattern for layered polysilane or silicane (dotted line, denoted as $Si_6H_6$) and two calculated patterns. Random stacking of the layers is assumed in the lower calculation (dashed line). Peaks from the beryllium window are indicated. The peak at 23.5° also arises from the Be window. b) FTIR spectra for (a) siloxene isolated from the topochemical reaction of $CaSi_2$ with HCl under controlled conditions; and (b) layered polysilane obtained by rinsing siloxene with HF. a) Reproduced from ref. [27] with permission from Physical Review B, copyright 1993. b) Reproduced from ref. [29] with permission from Journal of Materials Chemistry, copyright 1997.

### D.2 Topotactic transformation of $CaGe_2$

Similar to $CaSi_2$, $CaGe_2$ can be topotactically reacted to form the germanium graphane analogues, or germananes. In 2000, Vogg, Brandt, and Stutzman reported that upon reaction in HCl, GeH can be prepared through the topotactic deintercalation of $Ca^{2+}$ from the $CaGe_2$ lattice and the formation of terminal covalent bonds with $H^+$.[50] In contrast to silicane, whose structure and absence of oxygen is often ambiguous, the structure and oxygen-free nature of GeH has been elucidated using a variety of experiments. Part of this is aided by the fact the $GeO_2$ is water soluble and easily removed, but $SiO_2$ is not. Using a combination of FTIR, TGA, and XPS, Bianco *et al.* has shown the complete absence of oxygen on the surface (**Fig. 6a**) using both H- and D- labelling.[51] From XRD, it is shown that the 6R $CaGe_2$ lattice constants (a=3.999 Å, c=5.10 Å/layer) slightly contract along the a-axis, and expand along the interlayer direction in GeH (a=3.971 Å c=5.51 Å/layer) with some degree of interlayer disorder. More recently, Rietveld analysis utilizing synchrotron X-ray data has been used to confirm the structure of the 6R GeH polytype (**Fig. 6b**).[52] Direct evidence of the layered structure and honeycomb framework has been further elucidated using X-ray PDF measurements which show distinct differences compared to bulk Ge.[53] The structural models of GeH and Ge are shown in **Fig. 7a** and **7b**, respectively. The scattering of GeH has a similar real space PDF compared to Ge, except with systematic absences at 5.66 Å, 7.35 Å, and 8.95 Å (**Fig. 7d**). In Ge, these distances correspond to scattering from pairs of Ge atoms in different (111) layers (**Fig. 7b, arrows**). All other peaks can be indexed to the Ge-Ge pairs within a single Ge(111) plane (**Fig. 7c**). The distance of the Ge atoms on a particular coloured ring from the central Ge atom in **Fig. 7c** corresponds to the same colour peak in the PDF of **Fig. 7d**. The large interlayer disorder of GeH prevents the observation of scattering between any interlayer Ge-Ge pairs.

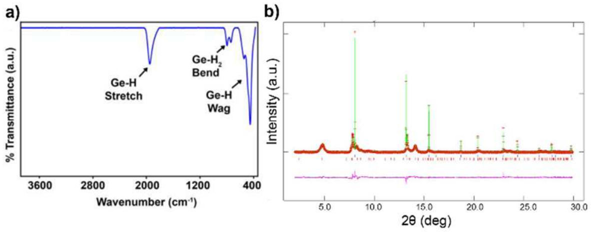

**Fig. 6.** a) Transmission-mode FTIR of GeH. b) Rietveld refinement results of 6R-GeH. containing 0.09 mole fraction of Ge as an internal standard. a) Reproduced from ref. [51] with permission from ACS Nano, copyright 2013. b) Reproduced from ref. [52] with permission from Chemistry of Materials, copyright 2018.

More recently, Cultrara *et al.* has shown that the the polytype of GeH is dictated by the layer stacking of the precursor Zintl phase.[52] Polytypism refers to the ability of a material to crystallize into different stacking motifs. In particular, the crystal structures of $EuGe_2$, α-$CaGe_2$, and β-$CaGe_2$, feature 1 puckered honeycomb layer of germanium atoms per trigonal unit cell (1T), 2-layers per hexagonal unit (2H), and 6-layers per Rhombohedral unit cell, respectively (**Fig. 8**). The polytype of the GeH formed was identical to the polytype of the initial Zintl phase. The layer stacking is retained between the Zintl phase and GeH in the low temperature topotactic process since conversion between different polytypes would require the layers to exfoliate, rotate by 30 degrees, and restack in a regular fashion.

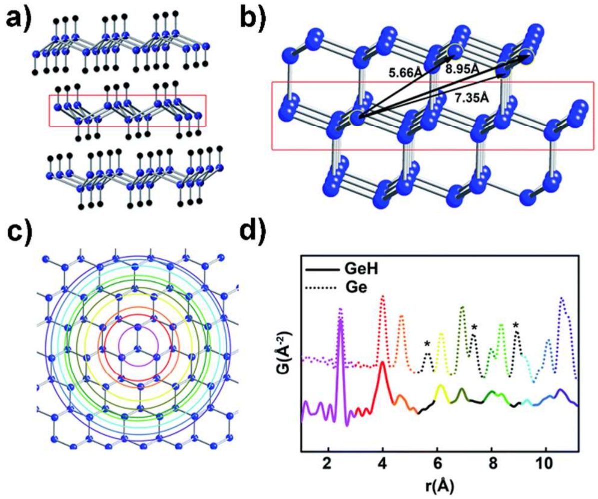

**Fig. 7.** Structural models of a) germanane and b) crystalline germanium, both of which have a hexagonal, $sp^3$-puckered layer of germanium atoms (boxes in a) and b)). c) A single (111) plane of crystalline germanium, representing a single layer of GeH. The distance of the germanium atoms on a certain colored ring from the central germanium atom corresponds to the same color peak in d). d) PDFs of GeH and Ge truncated at 10 Å to highlight the differences. The starred peaks correspond to the Ge–Ge pairs arrowed in b). Reproduced from ref. [53] with permission from Journal of Materials Chemistry C, copyright 2014.

Monolayers of hydrogen-terminated germanane have also been synthesized via electrochemical atomic layer deposition on Au(111) substrates. Initial three-electron reduction of aqueous $H_2GeO_3$ at pH of 4.7 first produces partial monolayers of a germanium hydroxide phase, that is subsequently reduced to form a material with the stoichiometry of GeH, which was determined via coulometry.[54] This adsorbed GeH material is surface-limited to 0.8 monolayers, and is flat and periodic based on STM measurements (**Fig. 9**). Further studies have suggested the possibility of forming ligand-free monolayer germanene using a similar process.[55, 56]

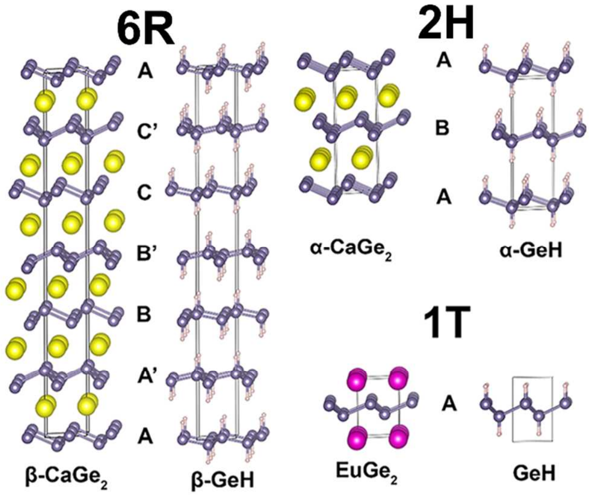

**Fig. 8.** Schematic representations of the structures of each precursor Zintl phase and their corresponding deintercalated phases. Intralayer covalent bonding between the germanium atoms (purple) is known for each phase and emphasized with cylinders drawn between closest neighbors, while the interactions between the calcium (yellow) or europium (magenta) atoms and the germanium atoms are mostly electrostatic, and no bonds are drawn. In the corresponding deintercalated phases, the hydrogen atoms terminating the layers are shown in pink. Reproduced from ref. [52] with permission from Chemistry of Materials, copyright 2018.

### D.3 Topotactic transformation of 2D Sn-containing Zintl phases

In contrast to Si and Ge, there is very little work on the formation of Sn-containing graphane analogues. First, $BaSn_2$ is the only crystalline material that features honeycomb networks of Sn.[57] This material was initially discovered in 2008 and found to crystallize into a 1T unit cell. We have recently synthesized single crystals of this material and found it to be among the most air-sensitive materials we have encountered. It starts to oxidize in an Ar-filled glovebox with <0.5 ppm $H_2O$ and $O_2$ within 15 minutes.[58] Our attempts to topotactically transform this Zintl phase into a 2D material have yielded only amorphous products.

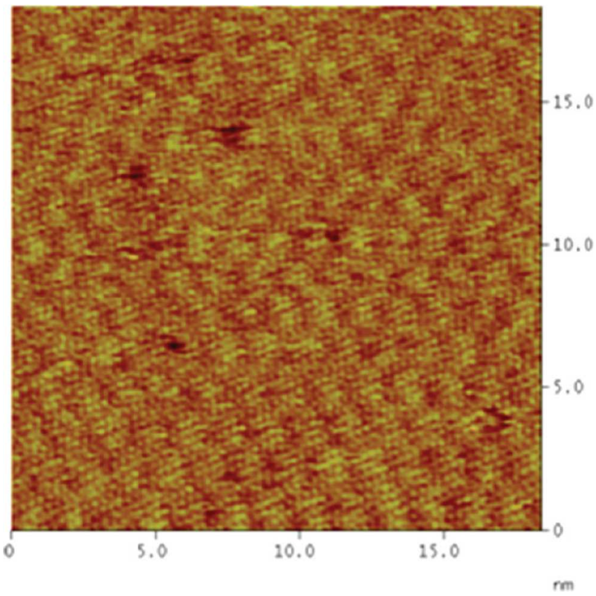

**Fig. 9.** STM image of Ge deposited on Au(111) at -800 mV in a 0.5M $Na_2SO_4$ + 1 mM $GeO_2$ pH 4.72 solution. Reproduced from ref. [54] with permission from Langmuir, copyright 2009.

While the pure 2D Sn phase remains elusive, the synthesis of crystals of 2D Ge/Sn graphane alloys have been successful, via the topotactic transformation of $CaGe_{2-2x}Sn_{2x}$ (x = 0–0.09) using aqueous HCl (**Fig. 10a,d**).[59] The combination of XPS, FTIR, and the large increase in interlayer spacing from XRD (**Fig. 10b,c,e**) indicate Sn is terminated with –OH while Ge is terminated with –H. This further reflects the propensity for oxidation of the more electropositive Sn atom compared to Ge. Finally, these $Ge_{1-x}Sn_xH_{1-x}(OH)_x$ materials oxidize upon exposure to air as evidenced by changes in their XPS and absorption spectra, but they can be reverted back to the original material upon washing with HCl.

### D.4 Direct Organic Functionalization Using Haloalkanes.

It has been shown that layered Zintl phases such as $CaGe_2$ can be topotactically transformed into GeH upon reaction with electrophilic species (i.e $H^+$). Recently a general approach to directly convert these layered Zintl phases into organic-functionalized germanane via the direct reaction with haloalkanes. In 2014, $GeCH_3$ was prepared via the reaction of $CaGe_2$ with $CH_3I$ (**Fig. 11a**) in a two-phase process.[53] This material features the same puckered honeycomb framework as the starting $CaGe_2$ Zintl phase, with a terminating $-CH_3$ group alternatingly above and below every atom in the framework. Again, the structure and composition has been confirmed using XRD, XPS, TGA, combustion analysis and FTIR. Isotopic labelling of the FTIR confirms $-CH_3$ termination, minimal –H termination (<10%), and lack of any Ge-OH or Ge–O stretch (**Fig. 11b**). Furthermore, the crystalline $GeCH_3$ shows intense red photoluminescence centered at ~1.7 eV (**Fig. 11c**).

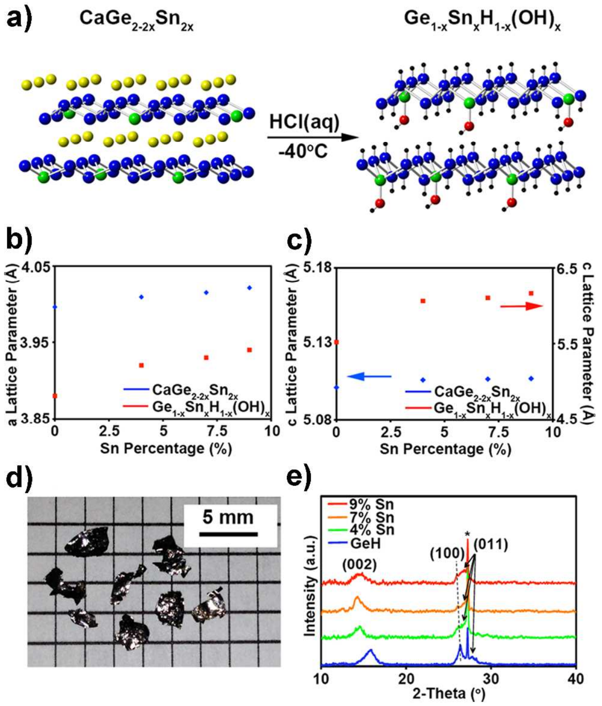

**Fig. 10.** a) Schematic of the topochemical deintercalation of $CaGe_{2-2x}Sn_{2x}$ to $Ge_{1-x}Sn_xH_{1-x}(OH)_x$ (Ca, yellow; Ge, blue; H, black; O, red; Sn, green). b) a/b- and c) c-lattice parameters of $CaGe_{2-2x}Sn_{2x}$ to $Ge_{1-x}Sn_xH_{1-x}(OH)_x$. d) Optical image of $Ge_{0.91}Sn_{0.09}H_{0.91}(OH)_{0.09}$ crystals on a 2.5 mm grid paper. e) Capillary mode powder XRD pattern of $Ge_{1-x}Sn_xH_{1-x}(OH)_x$ (x = 0–0.09). The internal Ge standard is labeled with an asterisk (*). Reproduced from ref. [59] with permission from Chemistry of Materials, copyright 2014.

Recently, a one pot methodology to prepare $GeCH_3$ has been established, which further increase the ratio of $-CH_3$:–H to ~95:5.[60] Here, the haloalkane, the Zintl phase, and specific equivalents of $H_2O$, and $CH_3CN$ solvent are all combined. This approach has led to the preparation of a large variety (>10) of organic terminated germanane derivatives (**Table 2**).[61] It is important to note that for small enough ligands such as $-CH_3$, $-CH_2OCH_3$, and $-CH_2CH=CH_2$, close to 100% of the germanium atoms are terminated with the organic ligand with minimal hydrogen.

Other topotactic reactions with these layered Zintl phases have been explored, but they have not necessarily led to the formation of different ligand terminated graphane analogues. For instance, Ramachandran *et al.* reported that the reaction of $CaSi_2$ with HF ultimately dissolves the Si network, leading to

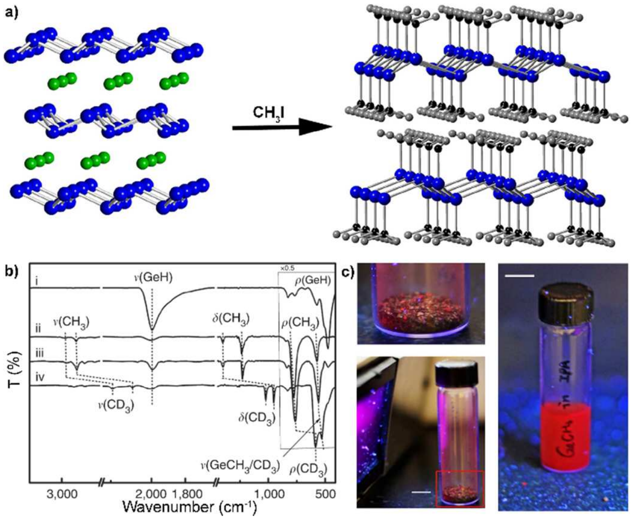

**Fig. 11.** a) Schematic illustration of conversion of CaGe$_2$ (left) into GeCH$_3$ (right). b) FTIR spectra of GeH (i), GeCH$_3$ (ii), Ge$^{13}$CH$_3$ (iii) and GeCD$_3$ (iv). The intensity of the four spectra are all multiplied by 0.5 in the range of 400–900 cm$^{-1}$. c) Images of GeCH$_3$ photoluminescence of crystals (left) and in suspension in isopropanol (right), upon illumination with a handheld 365 nm light. Scale bars, 1 cm. Reproduced from ref. [53] with permission from Nature Communications, copyright 2014.

the formation of CaF$_2$ platelets (**Fig. 12**).[62] In other work, CaSi$_2$ crystals were reacted in a BF$_4^-$ containing ionic liquid [BMIM][BF$_4$] (1-butyl-3-methylimidzolium tetrafluoroborate) at 300 °C, during which BF$_4^-$ decomposed into fluoride ions, which intercalated into the CaSi$_2$ crystal.[63] Based on transmission electron microscopy (TEM), the resulting CaSi$_2$F$_{0.6\text{-}2.0}$ product was heterogeneous, and consisted of layers of different thicknesses of CaF$_2$ layers, that separated different thicknesses of “silicene.” (**Fig. 13**). A common structural motif formed within the materials was a bilayer of “silicene” (**Fig. 13f**). Analogous bilayer germanenes were observed when [BMIM][BF$_4$] was reacted with CaGe$_2$.[64]

## E. Covalent Modification of Group 14 Graphanes

As discussed in the previous section, 2D GeH and SiH have been reported from the topotactic transformation of layered Zintl phases. These materials are structurally analogous to Si/Ge(111) surfaces. Consequently, the methods used to functionalize these (111) surfaces have been explored in these 2D graphane analogues. In this section, we discuss the successful routes that have been established for replacing –H termination on these 2D materials with different ligands, specifically those which utilize organoamines, Grignard chemistry, hydrosilylation, and hydrogermylation. These 2D materials have been found to exhibit much different reactivities than Si/Ge(111) surfaces. Furthermore, free-radical based mechanisms often amorphize these materials.

**Fig. 12.** CaF$_2$ nanosheets: a) TEM image shows the rectangular CaF$_2$ nanosheets and irregular CaF$_2$ particles. Inset: selected area electron diffraction arising from the cubic CaF$_2$ crystal structure. b) High-resolution TEM image of a single CaF$_2$ nanosheet displaying lattice fringes matching the (111) plane. c) Powder XRD pattern for CaF$_2$ nanosheets with reference pattern for CaF$_2$ d) Reaction schematic for the formation of CaF$_2$ nanosheets from CaSi$_2$ through interlayer confinement and templating effects.

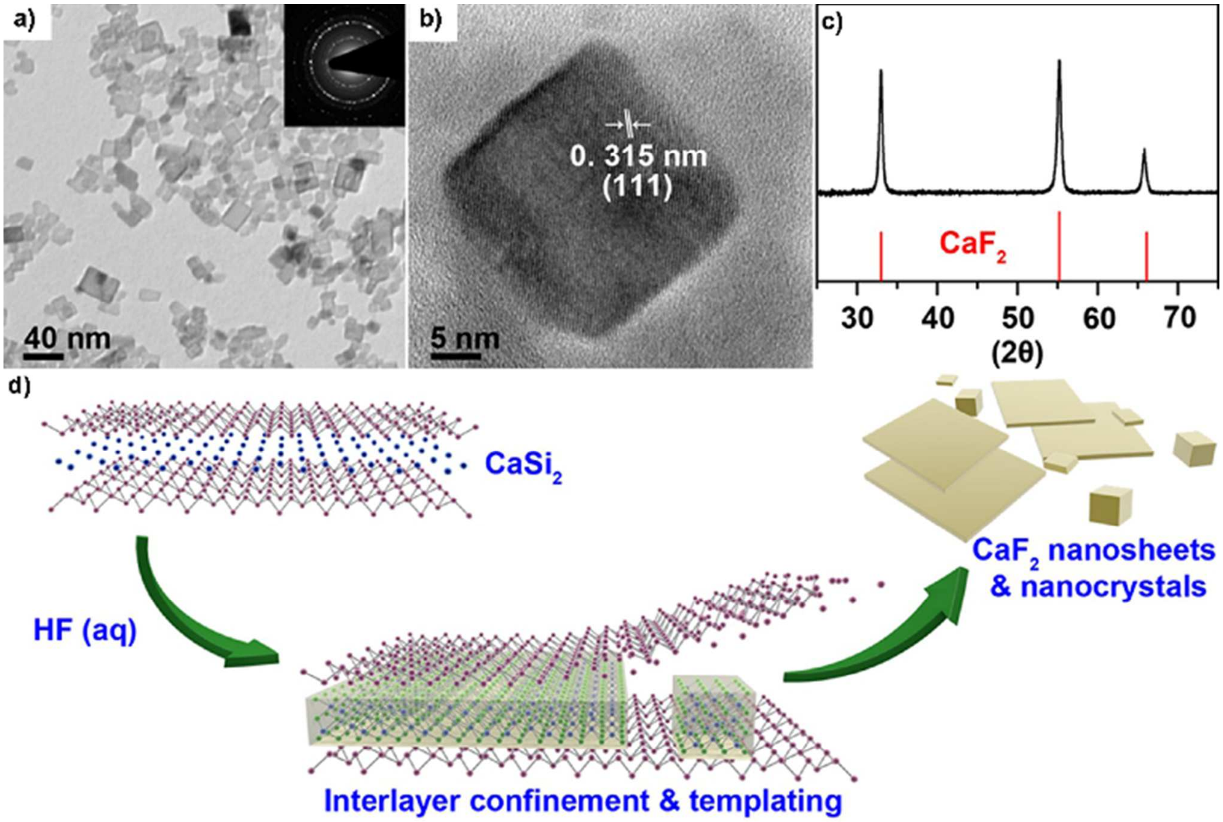

Reproduced from ref. [62] with permission from Chemistry of Materials, copyright 2016.

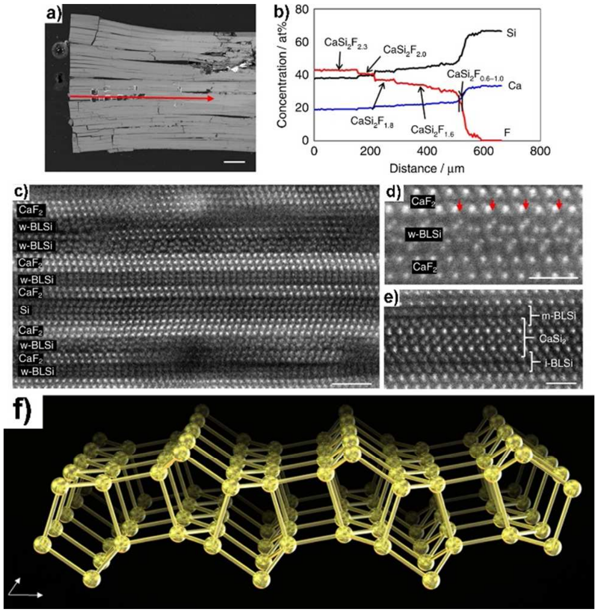

**Fig. 13.** a) Cross-sectional back scattered electron image of the crystal grain including $CaSi_2F_x$ compound. b) Electron probe microanalyzer quantitative line analysis result along the red arrow in a). c) High angle annular dark field scanning transmission electron microscopy (HAADF-STEM) image taken from a region with $CaSi_2F_{1.8}$ in b); the strip contrast corresponds to Si (dark domain) and $CaF_2$ (bright domain) planar crystals. d) An enlarged HAADF-STEM image taken from a region with $CaSi_2F_2$ in b); red arrows indicate an F-vacancy site. e) HAADF-STEM image taken from a region with $CaSi_2F_{0.6-1.0}$ in b); bright dots, corresponding to the projected atomic positions of the bilayer silicene can be observed in the image. f) Schematic illustration of one such bilayer silicene atomic structure. Reproduced from ref. [63] with permission from Nature Communications, copyright 2016.

### E.1 Hydrosilylation of SiH to SiR

Hydrosilylation has been reported as a viable strategy for replacing the –H termination on SiH with organic substituents. First, in 2012 Nakano *et al.* published that 1-hexene can insert into the Si–H bond using a $H_2PtCl_6{\bullet}6H_2O$ catalyst.[65] The FTIR shows alkane termination, along with Si-O peaks from 1000-1100 cm$^{-1}$. Furthermore, based on the XRD pattern (**Fig. 14**), the structure transforms from a hexagonal unit cell with a=3.83 Å and an expanded c-lattice of c=6.3 Å into a material that is almost completely amorphous with a weak, spurious reflection. No direct quantification of the percent surface coverage was investigated.

More recently, Helbich *et al.* developed a radical-initiated hydrosilylation process for functionalizing SiH and showed that a variety of alkenes and alkynes could be substituted on the surface. They compared 4-decylbenzene diazonium tetrafluoroborate (DDB) as a radical initiator, thermal initiation (130 °C), and no radical initiator at room temperature.[66] They showed using a combination of FTIR, TGA, and Nuclear Magnetic Resonance (NMR) data that all three initiators can produce some degree of organic termination. Our quantification of their TGA data, (assuming mass loss corresponds to complete removal of the dodecyl groups) estimated that no-radical initiator, DDB, and thermal initiation led to surface coverages of 9%, 19%, and 25% ligand termination, respectively. Their FTIR also supports evidence of partial oxygen termination.

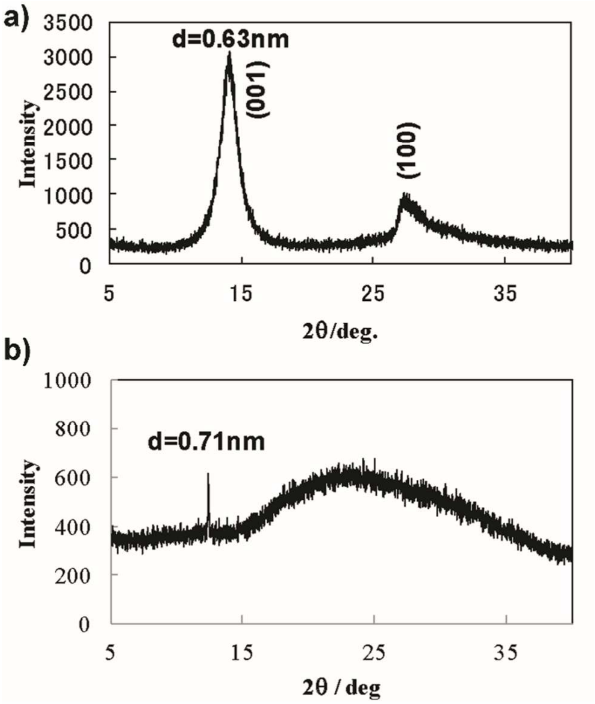

**Fig. 14.** XRD patterns of a) layered polysilane SiH and b) hexyl layered polysilane $Si(CH_2)_5CH_3$. Reproduced from ref. [65] with permission from Journal of the American Chemical Society, copyright 2012.

Finally, a Lewis acid catalyzed hydrosilylation approach to covalently modify these 2D silicon graphane materials with alkanes, esters, and vinyl silane approach has been reported.[48] Different Lewis acid 3-coordinate boron or aluminum catalysts, including $BH_3{\bullet}S(CH_3)_2$, $BF_3$, $B(C_6F_5)_3$, and $Al(C_6F_5)_3$ were all shown to be viable catalysts. In the proposed mechanism for this reaction, the Lewis acid catalyst first abstracts a hydride from the Si-H bond, to form a $Si^+$ silylium type surface species (**Fig. 15**). This species then reacts directly with the unsaturated ligand, to form a Si-C bond and producing a carbenium intermediate. The carbenium ion then abstracts a hydride from the hydride-Lewis acid adduct, ultimately producing the alkene or alkane-terminated surface. From our extrapolation of the reported TGA analysis, which assumes that annealing above 600 °C results in a material that is 100% Si, the relative density of organic termination ranges between 4 and 11% (**Table 2**). The ligand coverage of 1-dodecene using these Lewis acid catalysts was lower than that which was observed using the aforementioned thermally initiated hydrosilylation method.

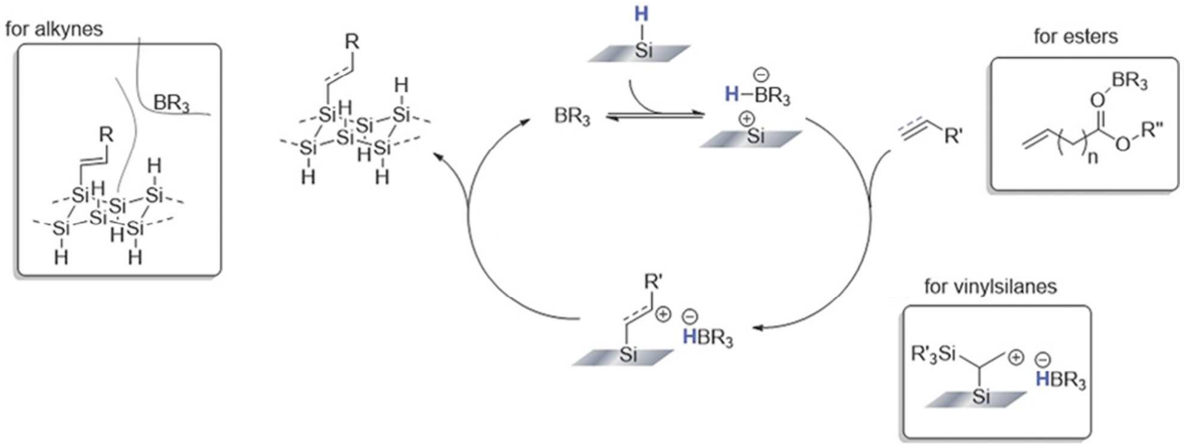

**Fig. 15.** Proposed mechanism exemplified for borane catalyzed hydrosilylation of SiH and unsaturated substrates. (Top) Preactivation of the SiH surface by the formation of a silylium type surface species. (Right) Subsequent direct addition of the unsaturated substrate to the silylium ion and trapping of the carbenium species by the boron based hydride. (Left) Reaction of the carbenium ion with the hydride regenerates the catalyst and renders functionalized surface. (Right bottom) Silicon atoms stabilize the positive charge in beta position and addition therefore induces a higher reactivity. (Right top) The carbonyl group of esters coordinates to the Lewis acid diminishing its catalytic reactivity. (Left box) Alkynes render alkene functionalized surfaces that exhibit a higher steric demand and thus prevent further surface functionalization. Reproduced from ref. [66] with permission from Wiley-VCH, copyright 2016.

### E.2 Hydrogermylation of GeH to GeR

Recently, H. Yu, *et al.* reported that GeH sheets can be functionalized with dodecene via both a radically-induced and thermally-induced hydrogermylated process (**Fig. 16**).[67] Both methods required a suspension of GeH sheets via bath ultrasonication, and either the addition of azobis(isobutyronitrile) as a radical initiator, or via heating in neat 1-dodecene at 190 °C. From the Ge:C XPS intensities, they estimated that the radical induced hydrogermylation process resulted in 55% of Ge sites that were ligand terminated (close to the 50% maximum reported ligand density on Ge(111))[10] whereas the thermally induced reaction resulted in 103% termination. This high density was attributed to partial oligomerization of the ligand. The TEM evidence suggests that both processes result in the partial fusion of the single-atom thick GeH layers to form bilayer and trilayers. In addition, the full width at half maximum (FWHM) of the main Ge-Ge Raman modes become much broader (>50 $cm^{-1}$) after both functionalization methods, which is indicative of partial amorphization (**Fig. 16b**). Further evidence of amorphization is apparent from the red-shifting of the absorbance spectra from a ~1.7 eV band gap in GeH to 1.5 and 1.1 eV for the radically-induced and thermally-induced processes, respectively (**Fig. 16c**). The signatures of amorphization will be discussed in greater detail in **section G.3**.

### E.3 Amination of SiH to SiNR

Organoamine functionalization of Si(111) has been accomplished via the dehydrohalogenation of Cl- and F-terminated Si(111) surfaces. There is no direct reaction between Si(111)–H surfaces and organoamines. Interestingly, organoamine substitution of SiH can be accomplished via direct reaction with organoamines to produce materials with both single Si–NHR and Si–(NR)–Si, along with hydrogen evolution (**Fig. 17**).[68, 69] TGA evidence indicates a functionalization density of ~70%. Changes in interlayer spacing with alkyl chain length using XRD indicates that these alkylamines are tilted at an angle of ~47 degrees. These organoamine-terminated silicanes are readily soluble in chloroform, oxidized in air but thermally stable up to ~150 °C. The fact that amination occurs via direct reaction with SiH is a testament to differences in reactivity between these 2D materials and Si(111).

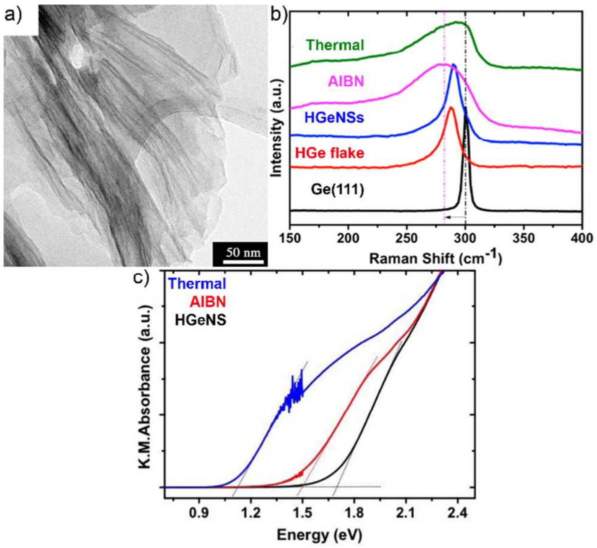

**Fig. 16.** a) Brightfield TEM of dodecyl terminated Ge nanosheets. b) Raman spectra highlighting the narrow FWHM of the $E_2$ mode of Ge(111) (black), GeH flakes (red) and dispersed GeH nanosheets (blue), and the broad dodecyl terminated germanane nanosheets prepared using azobisisobutylnitrile radical initiators (pink) or thermal initiators (green). c) Diffuse reflectance absorbance spectra of GeH flakes (black), radically induced dodecyl-terminated germanane (red), and thermally induced dodecyl-terminated germanane (blue). Reproduced from ref. [67] with permission from Chemistry of Materials, copyright 2018.

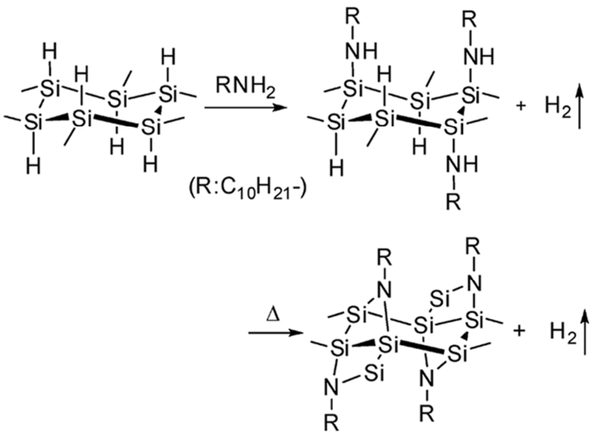

**Fig. 17.** Proposed reaction scheme for the synthesis of *n*-decylamine terminated silicane. Reproduced from ref. 46 with permission from Journal of the American Chemical Society, copyright 2010.

### E.4 Grignard reaction of SiH to SiH$_4$Ph$_2$

Another reported approach that can be utilized to prepare organic-terminated silicane is the direct reaction of Grignard reagents with SiH. In contrast to Si(111), where a halogenation step is first required, Sugiyama *et al.* reported that there is a direct reaction between PhMgBr and HF-treated SiH.[70] Using $^1$H NMR, the authors estimate that 2D sheets having a stoichiometry of SiH$_{0.67}$Ph$_{0.33}$ are prepared, and that this material is resistant to oxidation. It is hypothesized that the hydrophobic nature of the phenyl group improves the stability against oxidation. Despite the large number of Grignard reagents that are commercially available, this remains the only report of a group 14 graphane analogue that has been functionalized using this process.

## F. Covalent Modification of Other 2D Materials

The ability to covalently graft hydrogen and organic ligands onto many other families of 2D materials such as graphene, transition metal dichalcogenides, and phosphorene have also been explored in recent years. With the exception of graphene in which the C-C π-bonds can be functionalized to form C-R σ-bonds, these materials do not have the propensity to form covalent linkages on every atom. In contrast many of these "functionalized" 2D materials feature much lower ligand densities than the group 14 graphanes. In these other 2D materials, these ligands can be considered more as "dopants" rather than as a thermodynamic requirement for maintaining the stability of the framework. Here, we briefly highlight the families of covalently modified 2D materials that have been created experimentally. We compare the ligand functionalization density of these materials with the group 14 graphanes. For additional information on functionalization of graphene and transition metal dichalcogenides, we refer the reader to numerous recent reviews.[72-75]

**Table 2.** Reported ligand terminated 2D SiR and GeR surfaces, with the measured ligand density, and synthetic method. HI refers to the direct topotactic transformation using haloalkanes, HS refers to hydrosilylation, A refers to amination, HG refers to hydrogermylation. Quantitative determination of the Ligand Density was determined via combustion analysis unless labelled with a †=TGA assuming all residual mass is Si, $^{\times}$=XPS

| Ligand | Ligand Density | Synthesis Method | Ref. |
|---|---|---|---|
| | ***2D SiR*** | | |
| $-(CH_2)_5CH_3$ | -- | HS | 66 |
| $-(CH_2)_{11}CH_3$ | ~25%$^{\dagger}$/11%$^{\dagger}$ | HS/LA | 66, 48 |
| $-CH=CH(CH_2)_9CH_3$ | -- | HS | 66 |
| $-(CH_2)_9CH_2OH$ | -- | HS | 66 |
| $-CH=CH(CH_2)_7CH_3$ | 4%$^{\dagger}$ | HS | 48 |
| $-(CH_2)_2Si(CH_3)_3$ | 11%$^{\dagger}$ | HS | 48 |
| $-(CH_2)_{10}COOEt$ | 7%$^{\dagger}$ | HS | 48 |
| $-(CH_2)_2COOtBu$ | 7%$^{\dagger}$ | HS | 48 |
| $-C_6H_5$ | 33% $^{\times}$ | Grignard | 70 |
| $-N(CH_2)_{15}CH_3$ | -- | A | 68 |
| $-N(CH_2)_{11}CH_3$ | -- | A | 68 |
| $-N(CH_2)_9CH_3$ | -- | A | 68 |
| $-N(CH_2)_5CH_3$ | -- | A | 68 |
| $-N(CH_2)_3CH_3$ | -- | A | 68 |
| $-N(C_6H_5)$ | -- | A | 68 |
| $-N(CH_2)_2N-$ | -- | A | 68 |
| $-N(CH_2)_3N-$ | -- | A | 68 |
| $-N(CH_2)_6N-$ | -- | A | 68 |
| $-N(CH_2)_{12}N-$ | -- | A | 68 |
| $-N(CH_2)_{12}COOH$ | -- | A | 68 |
| | ***2D GeR*** | | |
| $-CH_3$ | 95(2)% | HI | 53, 60, 61, 71 |
| $-CH_2OCH_3$ | 105(7)% | HI | 61 |
| $-CH_2CH=CH_2$ | 102(3)% | HI | 61 |
| $-CH_2CH_3$ | 69(9)% | HI | 61 |
| $-(CH_2)_2CH_3$ | 50(1)% | HI | 61 |
| $-(CH_2)_3CH_3$ | 34(1)% | HI | 61 |
| $-(CH_2)_6CH_3$ | 60(9)% | HI | 61 |
| $-CH(CH_3)CH_2CH_3$ | 14(2)% | HI | 61 |
| $-CH_2C_6H_5$ | 31(6)% | HI | 61 |
| $-CH_2I$ | 59(1)% | HI | 61 |
| $-(CH_2)_{11}CH_3$ | 55%/100%$^{\dagger}$ | HG | 61 |

### F.1 Graphene to Hydrogen- and Fluorine-terminated Graphane

The hydrogenation of graphene to graphane was first reported in 2009 by Elias *et al.* Isolated layers of graphene were exfoliated onto a SiO$_2$/Si substrate, and hydrogenated via a hydrogen plasma that was kept 30 cm away from the discharge zone to prevent any damage by energetic ions.[76] The resulting hydrogen-terminated graphane was insulating, and was stable at room temperature for many days. Upon hydrogenation, the Raman showed the emergence of new D and D’ modes, while retaining the existing G and 2D modes of monolayer graphene. Surprisingly, the *a*-lattice of graphene at 2.46 Å was observed to decrease to 2.42 Å after hydrogenation. While this might seem to contradict the expectation that the C–C bond length will increase from ~1.42 Å in graphene to ~1.54 Å in graphane, it is consistent when considering the out-of-plane puckering of C atoms and a change in the C-C-C bond angle from 120$^o$ in sp$^2$ graphene to ~103.6$^o$ in sp$^3$-graphane. Quantitative determination of the % H termination was not established. After dehydrogenation via annealing at 450 $^o$C in Ar, the original metallic state returned.

A solution-phase route that converts graphene to graphane ($CH_x$) was reported by Schaefer *et al.*[77] This process utilized the Birch-type reaction sequence in which graphite was first intercalated with Li metal in liquid $NH_3$ at -78 $^o$C (**Fig. 18**). Subsequently, 10 eq. water was added to the reaction mixture, to serve as the proton source. The graphane flakes were separated via filtration. This process produced amorphous, mostly H-terminated graphane, with trace amounts of $–NH_2$ termination and LiOH that remained in the product. In the TGA-Mass spectrometry analysis, there was an appreciable (~18%) mass loss observed at 450 $^o$C, that coincided with the formation of $H_2$ as well as –OH and $H_2O$. This mass loss is much larger than the expected value of 8% for stoichiometric CH. This additional weight loss complicates quantitative determination of the degree of hydrogen termination. This material had a broad yellow fluorescence with UV excitation, that was attributed to the presence of isolated, randomly-sized nanographene domains (**Fig. 18**).

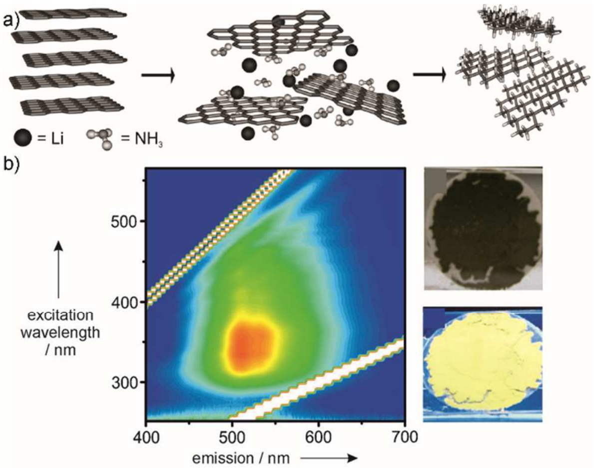

**Fig. 18.** a) Birch-type wet-chemical hydrogenation or deuteration of graphene, which was prepared from graphite with isotopically pure solvents and quenching reagents: First; $NH_3/ND_3$, Li, 2 h; Second; $H_2O/D_2O$. b) Emission/excitation map of $CH_x$ (with increasing intensity from blue to red). Images of filtered $CH_x$ before (above) and during excitation (below) with a handheld UV lamp (366 nm). Reproduced from ref. [77] with permission from Angewandte Chemie Int. Ed., copyright 2013.

Strategies for functionalizing graphene with halogens, including –F, –Cl, –Br, and –I, have also been developed.[78] These techniques oxidize graphite in the presence of halogenating agents. Methods of functionalization have included direct gas fluorination with $XeF_2$, plasma generated from either $F_2$ or $CF_4$, and photochemical fluorination generated from polymeric fluorocarbons (**Fig. 19**). These halogen atoms are excellent spectroscopic probes for determining the quantitative degree of functionalization. For instance, stoichiometric fluorination can occur using a variety of routes, whereas the other halogens have $CX_x$ stoichiometries of $x<0.43$.

### F.2 Organic Functionalization of Graphene

Over the last decade, there have been thousands of reports and many excellent methodologies on the functionalization of the basal-plane of graphene as well as graphene oxide.[73] Graphene oxide is formed by the oxidation of graphite in $HNO_3$ and $H_2SO_4$ acid and features a variety of oxygenated species on the basal plane and edges, including epoxides, carboxylic acids, and alcohols. There are many conventional organic reactions that allow for the covalent functionalization of these oxygenated species. The basal plane of graphene is structurally similar to the group 14 graphane analogues discussed here. Thus, we will briefly review strategies towards π-orbital functionalization of graphene, rather than graphene oxide.

The methodologies for direct covalent functionalization of graphene typically entail the reaction with radical species including nitrene, carbene, and aryl intermediates. (**Fig. 20**) The most common reagents to graft aryl substituents onto the surface are aryl diazonium salts. In basic or neutral conditions a dinitrogen molecule is eliminated leaving behind an aryl radical, followed by electron transfer from the graphene to form a covalent bond (**Fig. 20a**). For instance, Bekyarova *et al.* showed that (p-nitrophenyl)diazonium tetrafluoroborate reacts directly with the graphene surface. They quantified the density of nitrophenyl substituents that were grafted electrochemically, and came to an estimation of ~$10^{15}$ molecules/cm$^2$.[79] This functionalization density has been previously observed with highly ordered pyrolytic graphite, and corresponds to ~32% of the C atoms being functionalized with a ligand.[80] This is close to estimates of the highest density that aryl groups can pack onto a graphitic sheet considering the steric bulk of the ligands.[42]

Nitrene generating reagents have also been explored for functionalizing graphene. Nitrenes are reactive intermediates that are generated either thermally or photolytically from alkyl or aryl azides, respectively. These species participate in a [2+1] cycloaddition with the basal plane of graphene to form a benzazirine (**Fig. 20b**).[81, 82] For instance, He *et al.* demonstrated that a wide variety of alkyl nitrenes could be grafted onto graphene.[83] Furthermore, the functionalization density ranges between 1 ligand per 32 to 53 carbon atoms (2-3% coverage).[84, 85]

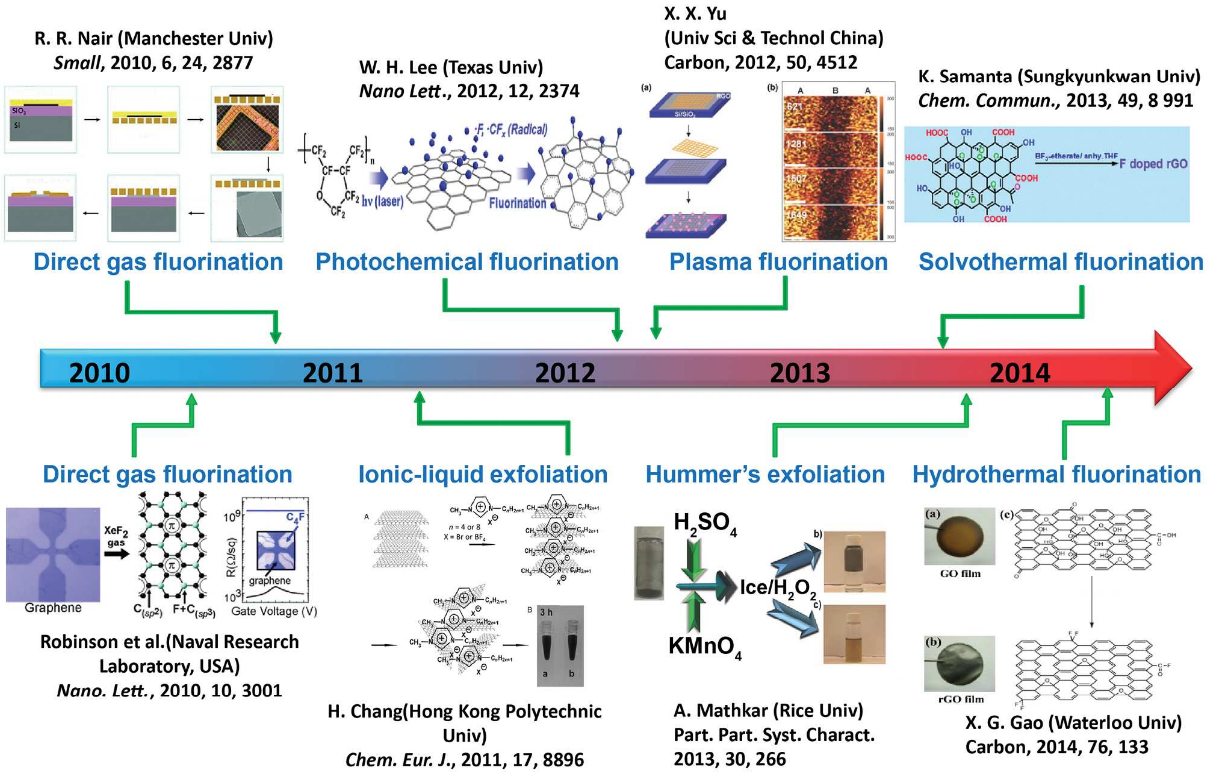

**Fig. 19.** Timeline showing recent synthetic methods regarding fluorinated graphene. Reproduced from ref. [78] with permission from Advanced Science, copyright 2016. Reproduced from ref. [86] with permission from Small, copyright 2010. Reproduced from ref. [87] with permission from Nano Letters, Copyright 2010. Reproduced with permission from ref. [88] with permission from Carbon. Copyright 2014, Reproduced with permission from ref. [89] with permission from Chemical Communications, Copyright 2013. Reproduced with permission from ref. [90] Copyright 2012, Nano Letters. Reproduced with permission from ref. [91] with permission from Chemistry – a European Journal. Copyright 2011.

Finally, carbenes have been shown to undergo [2+1] cycloadditions with the basal plane of graphene. Carbene reagents are typically generated through the thermo- or photolysis of species such as diazirines or haloform (**Fig. 20c**). These intermediates are capable of directly reacting with the basal surface of graphene as well as existing O—H or N—H bonds. One report by Ismaili *et al.* utilized gold nanoparticles decorated with diazirines which generate carbenes photochemically that then bind to the graphene surface.[92] The ligand density of the gold nanoparticles on graphene was not quantified but TEM and UV-vis spectroscopy indicated a large density of nanoparticles on the basal plane. Sainsbury *et al.* reported the functionalization of the basal plane with dibromocarbene to create dibromocyclopropyl groups on the surface.[93] The dibromocarbene is generated from the decomposition of bromoform in biphasic aqueous/organic mixtures under basic conditions. TGA data were used to characterize the ligand density of dibromocyclopropyl groups on the graphene surface and indicated that 1 of ~37 carbons, or 3%, of the graphene was functionalized.

## F.3 Organic Functionalization of Transition Metal Dichalcogenides

Transition metal dichalcogenides have become a very popular family of 2D materials especially for applications ranging from catalysis to electronics to valleytronics. Consequently, there have been numerous reports on the covalent functionalization of these materials.[74] Most of these studies have focused on functionalization of the canonical transition metal dichalcogenide, $MoS_2$. $MoS_2$ typically crystallizes into a 2D network comprised of sheets of edge sharing $MoS_6$ trigonal prisms on account of the $Mo^{4+}$ $d^2$ electron count, with each

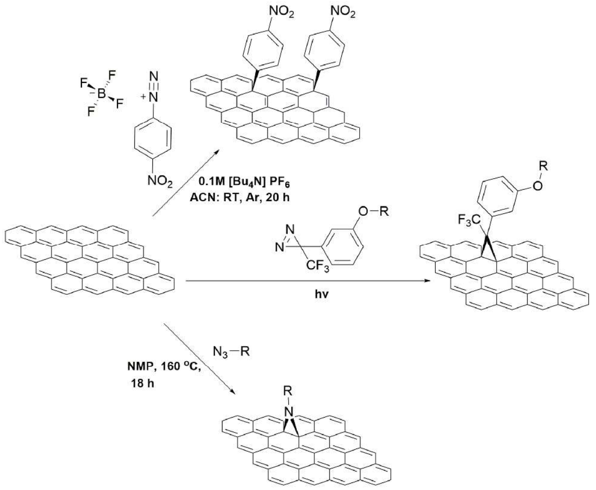

**Fig. 20.** Covalent functionalization of graphene using radical based mechanisms using reagents including (top) aryl radicals, (middle) carbenes, and (bottom) nitrenes.

layer held together by van der Waals bonding (**Fig. 21a**). The $MoS_2$ sheets crystallize into a hexagonal unit cell consisting of two layers (2H). Since, the chalcogen atoms tend to be saturated with a full octet and the transition metal is coordinatively saturated, the basal plane of $MoS_2$ tends to be inert to chemical functionalization. However, numerous strategies have been shown to partially functionalize these materials, including direct covalent functionalization on the basal plane and ligand conjugation to sulfur vacancies.

The covalent functionalization on $MoS_2$ typically first requires the transformation of the 2H-$MoS_2$ to the 1T-polytype followed by subsequent reaction with organohalides. The 2H-$MoS_2$ material is reduced by organolithium reagents such as n-butyl Li, to form $Li_xMoS_2$, with one full equivalent of Li yielding a trivalent $Mo^{3+}$. The $d^3$ electron count forces the sulfur atoms to rearrange around the $Mo^{3+}$ and into an octahedral coordination environment. The crystal structure changes into the 1T unit cell. This reduced $Li_xMoS_2$ can be re-oxidized in water to form $H_2$, while kinetically trapping and retaining the 1T-polytype. This re-oxidized 1T $MoS_2$ product is often referred to as "chemically exfoliated $MoS_2$." This 1T-polytype can then be reacted with electrophilic reagents such as organohalides, or diazonium salts to graft organic ligands to the surface (**Fig. 21**). For instance, Voiry *et al.* functionalized $MoS_2$ with organohalides including $CH_3I$ or iodoacetamide.[94] Using TGA, it was estimated that the degree of iodoacetamide functionalization corresponded to ~20% per Mo. The authors also extended this to functionalize $WS_2$, and $MoSe_2$, and found similar coverages. Knirsch *et al.* also showed that 1T-$MoS_2$ can be functionalized with organodiazonium reagents such as 4-methyoxyphenyldiazonium tetrafluoroborate.[95] Using a combination of XPS and TGA, the estimated % coverage corresponded to ~10-20% per Mo.

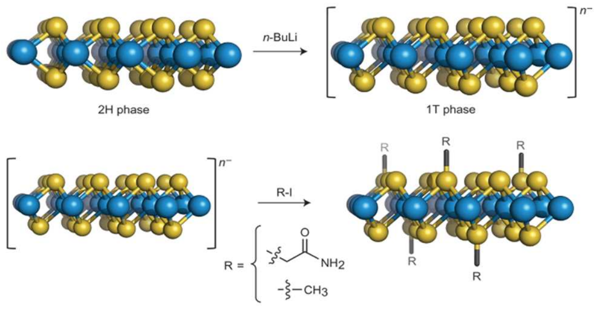

**Fig. 21.** a) The 2H phase of TMDs is converted to the 1T phase via lithiation using n-BuLi, and the 1T phase is negatively charged. $n^-$ indicates the excess charges carried by the exfoliated 1T phase nanosheets. b) The nanosheets are functionalized using 2-iodoacetamide or iodomethane. Reproduced from ref. [94] with permission from Nature Chemistry, copyright 2015.

The second route toward functionalization involves thiolation of chemically exfoliated $MoS_2$ prepared via the lithiation/re-oxidation route. Chou *et al.* showed that chemically exfoliated $MoS_2$ reacts with pegylated alkane thiols to produce a highly dispersible material with a much different ζ-potential.[96] FTIR indicates that the S-H bond is removed after reaction, and thus, the surfactant is bound as a thiolate anion. Zhou *et al.* extended this approach to the functionalization of smaller organic thiols such as 1-mercaptopropionic acid.[97] They estimated that 6-9% of the Mo sites were functionalized with thiolate ligands from TGA measurements.

### F.4 Organic Functionalization of Phosphorene

Recently, the surface functionalization of black phosphorus and phosphorene materials have been explored. Nominally, black phosphorus has a layered structure in which each P atom has a full octet, which includes a lone pair and 3 covalent bonds to its nearest neighbors. Interestingly, Ryder *et al.* showed that aryl diazonium chemistry can be utilized to functionalize the surface of black phosphorus with *p*-nitro-phenyl or *p*-methoxy-phenyl substituents.[98] The generated aryl radicals form new covalent bonds with the phosphorus atoms. According to DFT molecular models these correspond to 4-coordinate species that significantly distort the phosphorene framework, caused by electron transfer from the black phosphorus to the ligand (**Fig. 22**). While the quantification of the ligand coverage was not estimated, this functionalization coincides with an increase in air and $H_2O$ stability and p-type doping of the framework.

## G. Changes in Electronic Structure and Thermal Stability for Functionalized Group 14 Graphanes

As we have established in the previous sections, the group 14 graphane analogues are the materials that have the highest degree of surface functionalization since each surface atom requires a covalently bound ligand to remain stable. Consequently, the identity of the surface functionalization ligand will have a much greater impact on the properties of these 2D materials compared to any other 2D material family. Here we discuss how the electronic properties and the thermal stability change via ligand identity.

### G.1 Changes in Electronic Structure upon Functionalization

The changes in electronic structure that occur from silicon to silicene to hydrogen-terminated silicane, are representative for this family of 2D materials.[99] **Fig. 23** illustrates the transformation in electronic structure as single [111] layers are stretched apart to transform into silicene, as predicted via DFT. This band structure is calculated in hexagonal coordinates for simplicity. Bulk silicon is an indirect band gap semiconductor, in which each silicon atom has a full octet on account of 4-covalent σ bonds with its nearest neighbors. As the planes of Silicon atoms are pulled apart in the z-direction, the $p_z$ orbital overlap decreases, and consequently, the difference in energy between the σ and σ* orbitals decrease. Once the layers are far enough apart such that interlayer $p_z$ overlap is negligible (>10 Å), the system becomes semimetallic with a Fermi-Dirac like dispersion at the **K**-point, analogous to graphene. These layers are indeed isoelectronic to graphene as each Si atom possesses a half-filled $p_z$ orbital. They still exhibit the Fermi-Dirac dispersion despite the puckered geometry.

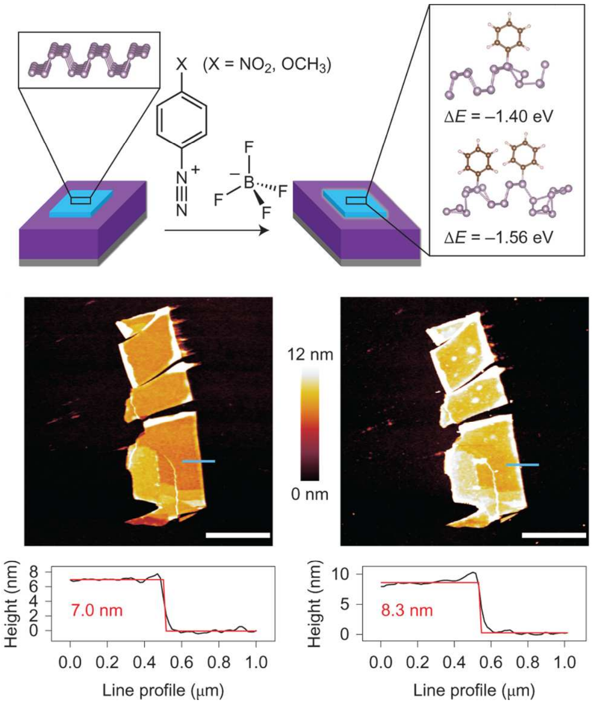

**Fig. 22.** (Top) Reaction scheme of benzene-diazonium tetrafluoroborate derivatives and mechanically exfoliated few-layer BP (light blue) on a Si (grey)/SiO2 (purple) substrate. The left inset shows the pristine structure of BP and the right inset shows DFT-calculated structures of the thermodynamically favoured covalent bonding of aryl groups to BP. The adsorption of aryl groups is predicted to produce BP lattice distortion. Carbon, brown; hydrogen, white; phosphorus, purple. The adsorption energy per aryl group is defined as ΔE= (E(n$C_6H_5$/BP) – E(BP) – E(n$C_6H_5$))/n, where n = 1 or 2 depending on the number of aryl groups. E(n$C_6H_5$/BP) is the energy of covalently bound aryl group(s) to BP, and E(BP) and E(n$C_6H_5$) are the initial energies of unassociated BP and aryl molecule(s), respectively. (Middle left) AFM micrograph of a BP flake prior to functionalization, along with the flake-height profile extracted along the blue line (Bottom left). (Middle right) AFM micrograph of the same flake after 30 minutes of exposure to 10 mM 4-NBD with the height profile extracted along the blue line (bottom right), which shows an increase in flake height that is attributed to the attachment of aryl groups. Scale bars, 2 µm. Reproduced from ref. [98] with permission from Nature Chemistry, copyright 2016.

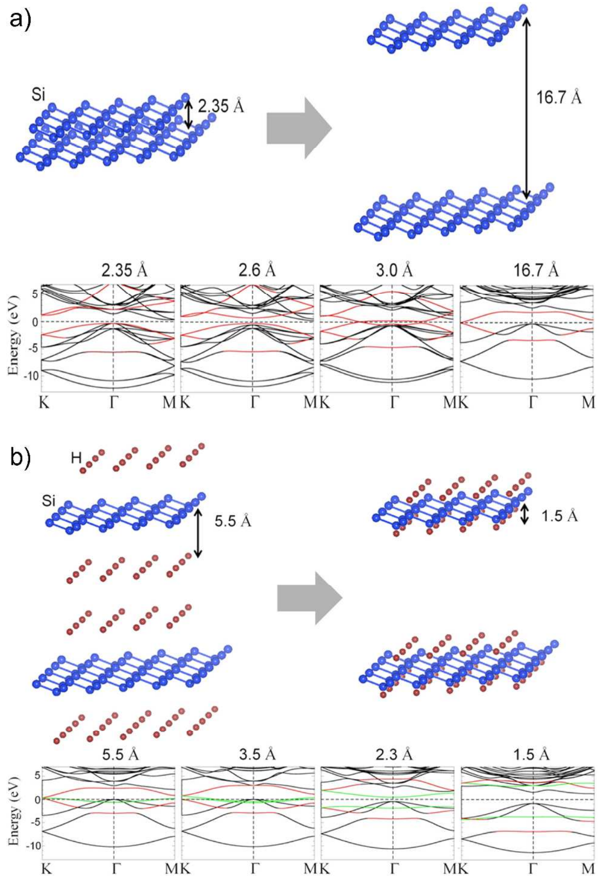

**Fig. 23.** a) Band structure evolution from silicon to silicene. b) Band structure evolution from silicene to silicane. Si $3p_z$ bands are shown in red. H-derived bands are shown in green. Reproduced from ref. [99] with permission from Journal of Applied Physics, copyright 2014.

Covalently grafting a surface ligand to the half-filled $p_z$ orbital in silicene will induce splitting of these Fermi-Dirac bands into bonding and antibonding bands. Fig. 23b, shows the changes in electronic structure as H-atoms approaches the silicene framework to form bonding and antibonding orbitals. The semimetallic nature is disrupted and the material becomes a semiconductor. The valence band maxima (VBM) at Γ and M both corresponding to bands originating from Si-Si bonding of the $p_x$ and $p_y$ orbitals. The conduction band minimum (CBM) at Γ corresponds to the Si-H σ* band, and the CBM at M is mainly $p_x$ and $p_y$ Si-Si σ*. In silicane the band gap is calculated to be indirect 2.94 eV since the CBM at M is slightly lower in energy than at Γ, whereas in GeH (**Fig. 24**) and SnH the CBM at Γ is lowest in energy and have direct band gaps. For instance, the direct band gap of GeH is predicted to be 1.56 eV, which has been confirmed via absorption and photoluminescence measurements.[51, 100] SnH has not been synthesized but is predicted to have a band gap of 0.25 eV.[101]

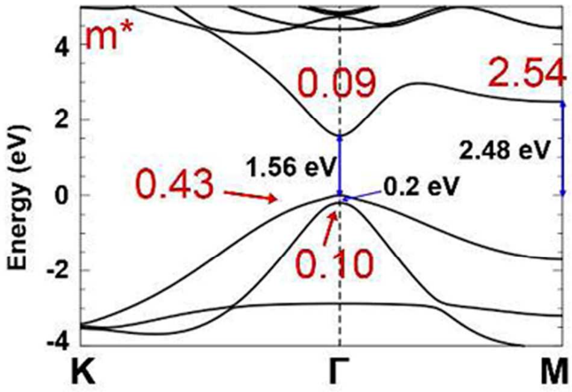

**Fig. 24.** Electronic band structure of an isolated single layer of GeH calculated using HSE-06 theory including spin-orbit coupling predicting a 1.56 eV direct band gap. The hole and electron effective masses for each extrema are indicated in red. Reproduced from ref. [51] with permission from ACS Nano, copyright 2013.

All of the orbital character in the CBM and VBM of these graphanes correspond to in-plane (Si/Ge/Sn)-(Si/Ge/Sn) $p_x$ and $p_y$ σ or σ* bonding character except for the CBM at Γ.[99] Therefore, the largest changes in energy at each of these extrema will occur via changing the in-plane bond lengths. Indeed, DFT studies on SiH showed that small changes in the Si-Si bond length more dramatically influence the magnitude and direct/indirect nature of the band gap compared to the Si-Si-Si bond angle and the Si-H bond length. This indicates that surface functionalization chemistry can most dramatically alter the electronic structure of these materials through their influence on the network bond lengths.

The anomalous photoluminescence properties of ligand terminated silicane illustrates the influence of surface functionalization chemistry on the optical properties and electronic structure of these 2D materials. First principles calculations of SiH using many different functionals predict that has an indirect band gap.[99, 102, 103] Using HSE-06 hybrid functionals which typically have an accuracy of <0.1 eV for Si and Ge semiconductors, SiH has an indirect gap of 2.94 eV from Γ to M and a larger direct gap at Γ of 3.14 eV.[104] However, as discussed previously, in almost all cases Si-O bonds are apparent in every reported almost all absorption and luminescence experiments on SiH materials show a 2.4 eV absorption onset, and also a broad photoluminescence centered at 2.4 eV. Additionally, lower-level first principles calculations using the local density approximation predict that half-hydroxide terminated $SiH_{0.5}(OH)_{0.5}$ will have a much lower 1.7 eV direct band gap at Γ.[101] This suggests that even a small amount of –OH termination may reduce the apparent band and may be responsible for photoluminescence. Clearly a more rigorous understanding on the influence of partial –OH termination is needed. Finally, many of the organic-terminated silicane materials photoluminesce at different wavelengths. The previously discussed amine functionalized silicane materials are reported to luminesce from 2.66 to 3.0 eV,[68, 69] the Grignard-functionalized $SiC_6H_5$ luminesces at 3.0 eV,[70] and the organic terminated hydrosilylation SiR products are reported to luminesce from 2.4 to 3.1 eV.[46, 48] Whether this photoluminescence corresponds to actual band edge emission or, again, a particularly emissive defect state for these different surface functionalized materials requires further exploration.

Thus far, the most systematic effort in understanding the influence of surface functionalization chemistry on the band gap of these group 14 graphane materials was established by Jiang *et al.*[61] Through the synthesis of over 10 different ligand-functionalized germanane materials, the interplay of ligand size and electronegativity on functionalization density, framework structure, and electronic structure was established (**Fig. 25**). Nearly uniform termination only occurs with the small ligands –H, $–CH_3$, $–CH_2OCH_3$ and $–CH_2CH{=}CH_2$. Substituting larger, more sterically bulky ligands onto the framework will lead to partial hydrogen termination. When a homogeneous distribution of different ligands are grafted onto the framework, the band gaps and Ge-Ge Raman shifts are dictated by their relative stoichiometry in a pseudolinear fashion similar to Vegard's law. Furthermore, increasing the density and homogeneity of ligand coverage causes these materials to exhibit more ideal 2D optoelectronic properties. For instance compared to $Ge(CH_3)_{0.90}H_{0.10}$, $Ge(CH_3)_{0.95}H_{0.05}$ has a more narrow band edge photoluminescence peak (FWHM=180 meV compared to 250 meV) and a sharper absorption onset that is much closer to the ideal step function of absorption predicted for a 2D direct band gap semiconductor by the Tauc-Davis-Mott expression (**Fig. 26a**).[60]

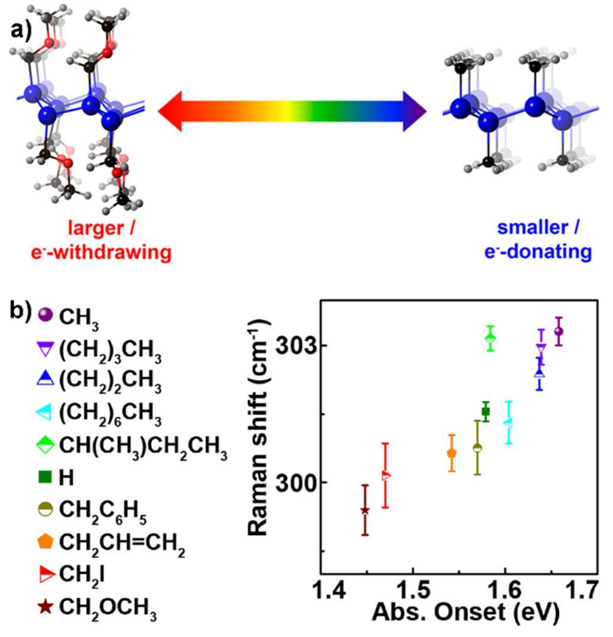

**Fig. 25.** a) Schematic illustration showing the influence of ligand size and electron-donating/withdrawing ability on red/blue-shifting of band gap. b) $E_2$ Raman shifts in ten

different ligand functionalized germananes plotted as a function of their absorption onsets. The error bars were obtained from the standard deviation of peak positions from 10 different spectra for each sample. Reproduced from ref. [61] with permission from Chemistry of Materials, copyright 2016.

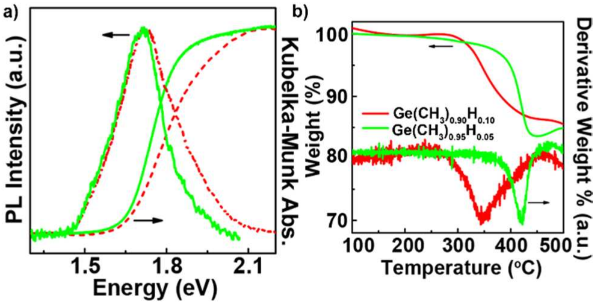

**Fig. 26.** a) DRA, and PL comparison between $GeCH_3$ prepared from the $Ge(CH_3)_{0.90}H_{0.10}$ after HCl treatment (red, dashed lines) and the $Ge(CH_3)_{0.95}H_{0.05}$ (green, solid lines). b) TGA (top, left axis) and differential TGA (bottom, right axis) of $GeCH_3$ synthesized from $Ge(CH_3)_{0.90}H_{0.10}$ (red) and $Ge(CH_3)_{0.95}H_{0.05}$ (green), respectively. Reproduced from ref. [60] with permission from Chemistry of Materials, copyright 2016.

Larger and more electronegative ligands expand the germanane framework, thereby lowering the band gap and Raman shift. In other words, the largest change in properties occurs with ligands that can be stoichiometrically grafted onto the framework. In total, the band gap can be broadly tuned by ~15% simply by substituting the identity of the organic ligand, from ~1.45 eV for the electron-withdrawing $–CH_2OCH_3$ group to 1.66 eV for the electron-donating $–CH_3$ substituent. These different organic terminated germananes are predicted to have direct band gaps and indeed show band edge photoluminescence.[61, 71] This highlights the power of functionalization chemistry to rationally tune the structure and band gap of 2D materials.

One additional method for tuning the electronic structure is to alloy the framework with different group 14 elements. This has been readily accomplished via the synthesis of precursor Zintl phases that feature alloys of these different elements. For instance, Vogg *et al.* established that topotactic deintercalation of $Ca(Si_{1-x}Ge_x)_2$ resulted in 2D materials in which Ge was terminated with H, and Si was terminated with different ratios of –H and –OH, depending on the alloy composition.[105, 106] In Si rich compounds (x<0.5) the stoichiometry was determined to be $Si_{1-x}Ge_x(OH)_{0.5}(H)_{0.5}$ using energy-dispersive X-ray spectroscopy and hydrogen effusion experiments. FTIR experiments indicated that the Si atoms were terminated by either –OH or –H in these Si-rich alloys. However, in Si poor alloys (x>0.5), the Silicon was exclusively terminated with –OH groups instead of –H, yielding a stoichiometry of $Si_{1-x}Ge_x(OH)_{1-x}(H)_x$. The band edge absorption was defined from the maximum slope above the absorption edge and varied from ~2.6 eV for $Si(OH)_{0.5}(H)_{0.5}$ to ~1.8 eV for GeH (**Fig. 27**). The Si rich samples (x<0.5) all had an absorption edge close to 2.8 eV, whereas the absorption edge linearly decreased in the Ge-rich samples when x>0.5. All samples exhibit a photoluminescence peak that is ~0.45 eV lower in energy than the defined absorption edge. Similarly, Arguilla *et al.* have shown that $Sn_{1-x}Ge_x(OH)_{1-x}(H)_x$ can be prepared via the topotactic deintercalation of $Ca(Sn_{1-x}Ge_x)_2$ for x<0.09.[59] In this case, the Sn atoms become terminated with –OH peaks, and the Ge atoms remain –H terminated. Here, the band gap was defined as the low energy tail of the absorption edge, and decreases from 1.59 eV for GeH down to 1.38 eV with 9% Sn. Together this shows that different group 14 elements exhibit different surface termination preferences, and that tuning of the band gap can be accomplished via the alloying of these elements together.

### G.2 Carrier Mobilities

The electron and hole carrier mobilities, defined as the speed of these carriers under an applied electric field, are the most significant properties of any material for electronic devices. For instance, a large carrier mobility allows for faster transistor switching, as well as the realization of quantized conduction phenomena such as the quantum Hall effect. The mobility of a carrier is inversely proportional to its effective mass. The effective mass itself is inversely proportional to its band curvature (i.e. the second derivative of the band structure). For room temperature, the maximum value of electron and hole mobilities for Si is 1,400 and 450 $cm^2\ V^{-1}s^{-1}$, respectively,[107, 108] and for Ge is 3,900 and 1,900 $cm^2\ V^{-1}s^{-1}$.[109, 110] The group 14 graphene analogues (graphene, silicene, germanene, and stanene) all feature a linear Fermi-Dirac dispersion from the half-filled $p_z$ orbitals. This causes these carriers to behave as though they have no effective mass, and in the case of graphene, can lead to field effect mobilities of ~200,000 $cm^2\ V^{-1}s^{-1}$, and the observation of the quantum Hall effect at room temperature.[1]

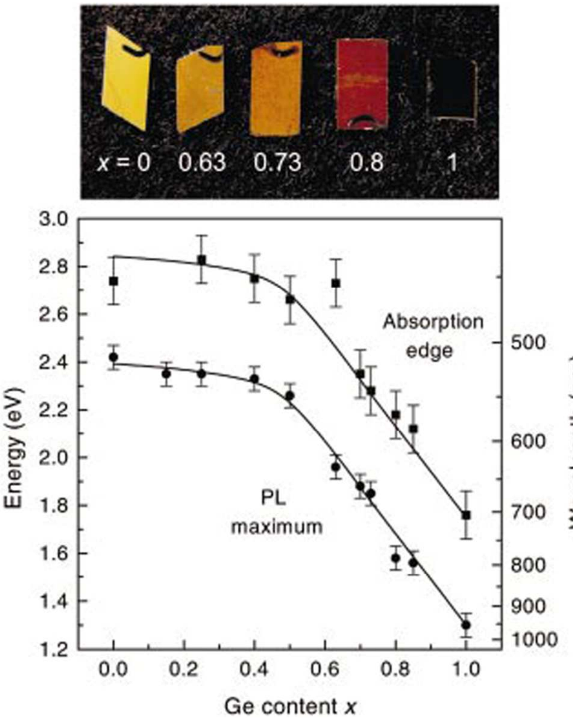

**Fig. 27.** Energy of the photoluminescence maximum and of the absorption edge of $Si_{1-x}Ge_x$ sheet polymers as a function of the Ge content *x*. The photograph shows the

visual appearance under white light of some of the sheet polymers studied. Reproduced from ref. [105] with permission from Applied Physics Letters, copyright 2001.

Once these 2D materials are functionalized with ligands, they transform back into semiconductors. While first principles simulations of the phonon-limited mobility have yet to be performed for SiH, the hole and electron effective masses are similar, and slightly larger than bulk Si.[111] Interestingly, first principles simulations predict that the room temperature electron mobility of germanane is 18,000 $cm^2\ V^{-1}\ s^{-1}$, which is 5x larger than that of bulk germanium.[51, 104] While one might expect that 3D materials will have greater band dispersions, lower effective masses, and consequently higher mobilities than 2D materials, this increase in mobility can be explained upon close inspection of the band structure of bulk Ge. In Ge, the CBM occurs at four equivalent L <111> valleys, and has a much higher effective mass ($m_e$*, L = 1.64 $m_0$) than the conduction band valley at Γ ($m_e$*, Γ = 0.041 $m_0$). Since GeH can be considered as hydrogen-terminated isolated (111) sheets of germanium, the dispersion along the L wavevector in the Ge Brillouin zone is effectively eliminated. Consequently, the new CBM in GeH has a much smaller effective mass (0.09 $m_0$) and a higher electron mobility. As expected, the hole effective masses in 2D GeH are greater than those in 3D Ge. To date, these values have yet to be confirmed experimentally, on part due to the difficulty in preparing large-domain defect-free materials, sufficient for transport. This will be discussed further in **section H.1**

### G.3 Thermal Stability, Conductivity, and Signatures of Amorphization

Along with tuning the electronic properties and band gap, organic functionalization also affects the chemical and thermal stability. To illustrate these changes, it is first worthwhile to monitor the changes in properties upon annealing GeH. TGA analysis of GeH indicates that H starts to desorb off the surface between 200-250 °C (**Fig. 28a**).[51, 53] Upon annealing in $H_2$/Ar at different temperatures, there is no obvious change in the XRD pattern until annealing at 150 °C, at which point there is small decrease in the c-axis spacing (**Fig. 28b**). Almost complete amorphization occurs at 175 °C according to the XRD pattern. Temperature dependent PDF measurements show that the amorphization process occurs at temperatures below 175 °C with a much more gradual onset. Upon annealing, there is a simultaneous increase in scattering intensity arising from Ge-Ge pairs in amorphous Ge, along with a dropoff in intensity from Ge-Ge pairs in a single GeH layer (**Fig. 28c**). We have found that absorption spectroscopy is the most sensitive analytical technique for detecting the amorphization of GeH. Amorphous germanium and hydrogenated germanium thin films typically have absorption onsets at energies that are lower than the band edge of 2D GeH, facilitating their detection. Indeed annealing GeH above 75 °C causes a red shift in the absorption by about 0.06 eV (**Fig. 28d**). The onset shifts to even lower energies upon annealing at higher temperatures. Finally, upon amorphization, the Raman intensity of both the $E_2$ and $A_1$ modes decrease, as observed when annealing above 75 °C (**Fig. 28e**). With decreasing domain size, and increasing defect density the FWHM of the Raman modes will increase appreciably.[67, 112] Similarly, the thermal amorphization of silicane materials have also been explored. For SiH, diffuse reflectance absorbance experiments indicate that amorphization occurs when annealing between 300 °C and 400 °C.[47]

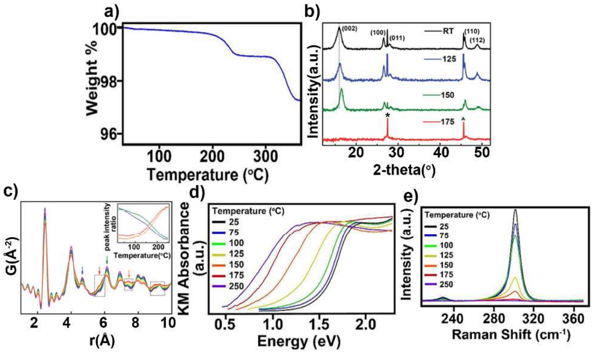

**Fig. 28.** a) TGA analysis of GeH. b) Temperature-dependence XRD GeH synthesized from concentrated HCl at -40°C. The starred peaks correspond to reflections from an internal Ge standard. The Miller indeces of each peak from GeH are pointed out. c) Temperature-dependent PDF of GeH from room temperature (purple) to 250 °C (red). The data are truncated at 10 Å to highlight the difference. Inset is the ratio of the intensity of different peaks (arrowed) to the peak at 4 Å. The colors of the arrows correspond to the colors of the curves in the inset. Reproduced from ref. [51] with permission from ACS Nano, copyright 2013. Reproduced from ref. [53] with permission from Journal of Materials Chemistry C, copyright 2014.

There have been relatively few studies on the thermal conductivity properties of these materials. Initial work by Coloyan *et al.* evaluated the in-plane thermal conductivity of micron-sized GeH flakes using a suspended electrode four-probe thermal transport measurement method.[113] The room temperature thermal conductivity was measured to be incredibly low, (0.53 ± 0.09 $W\ m^{-1}\ K^{-1}$). This is much lower than first principles simulations of the ideal crystalline GeH material (8.8 $W\ m^{-1}\ K^{-1}$). Furthermore, the observed increase in thermal conductivity with increasing temperature is indicative of extrinsic grain boundary scattering and defect scattering dominating over intrinsic phonon-phonon scattering. Indeed amorphizing this material further upon annealing at 195 °C, leads to a further decrease in thermal conductivity down to 0.29 ± 0.05 $W\ m^{-1}\ K^{-1}$.

Ligand termination profoundly influences the thermal stability of these materials. For instance, in $Ge(CH_3)_{0.90}H_{0.10}$ the amorphization onset as determined by diffuse reflectance absorbance increases appreciably to 200-250 °C.[60] Also, at this ligand density TGA analysis indicates that the $CH_3$ starts to desorb at ~300 °C (**Fig. 26b**). Increasing the coverage of $–CH_3$ termination to $Ge(CH_3)_{0.95}H_{0.05}$ further improves methyl desorption temperature to ~400 °C. This remarkable improvement in thermal stability highlights the necessity of optimizing functionalization to achieve complete covalent coverage.

## H. Prospective Applications of Functionalized 2D Materials

Here, we discuss some of the preliminary applications that have been explored in these covalently functionalized layered group 14 materials. In the past section we have shown that the electronic structure, optical properties, and thermal stability of the 2D framework are fundamentally different than 3D Si, Ge, and Sn and can be broadly tuned depending on the identity of the ligand and main group element. Most initial studies have focused on exploiting the inherent properties of the group 14 framework, for applications in electronics, optoelectronics, photocatalysis, batteries, and topological insulator applications. What has been less well explored with these materials are applications in which the ligand plays a more active role, such as in chemical and biochemical sensors or membrane technologies.

### H.1 Electronics and Optoelectronics

Group 14 semiconductors form the backbone of modern electronic technology. These 2D SiH, GeH, and SnH frameworks are predicted and in some cases observed to have much larger band gaps (2.4, 1.56, and 0.3 eV, respectively) than 3D Si, Ge, and Sn (1.12, 0.67, and 0.03 eV, respectively). Furthermore, the entire band structure becomes 2D in nature, and in the case of GeH, there is an increase in electron mobility. Consequently, initial studies characterized the in-plane and cross-plane electrical conduction properties in order to exploit these 2D derivatives into electronic and optoelectronic devices.

Brandt *et al.* first evaluated the electronic conductivity of the $SiH_{0.5}(OH)_{0.5}$ on ~3 mm crystallites.[114] At 250 $^{o}$C, the in-plane and cross-plane conductivity values were observed to be $10^{-11}$ and $10^{-14}$ $\Omega^{-1}cm^{-1}$, respectively, which are extremely resistive values. At room temperature the in-plane conductivity was extrapolated to be $10^{-19}$ $\Omega^{-1}cm^{-1}$. These incredibly low conductivity values could result from a lack of doping, imperfect crystallinity, and the presence of deep-level defects. The authors attributed this low conductivity mainly to the lack of doping. The activation energies based on the temperature dependence of conductivity were observed to be about half the band gap at ~1.2 eV, which is expected for an undoped semiconductor. When $SiH_{0.5}(OH)_{0.5}$ was annealed above 300 $^{o}$C it partially amorphized and the conductivity increased appreciably by a factor of ~1000x along the in-plane direction and ~10x along the cross-plane direction.

Recently, field effect transistors of nominally undoped, mechanically exfoliated GeH sheets were demonstrated by Madhunshankar *et al.*[115] The authors demonstrated ambipolar device behavior in both the electron and hole doped regimes. In the electron and hole channels on/off current ratios were observed to be $10^5$ and $10^4$, respectively, and the device mobilities at 77 K were 150 and 70 $cm^2$ $V^{-1}s^{-1}$, respectively. To date this represents the only reported field effect transistors fabricated with these group 14 graphane analogues.

The electronic properties of GeH when different group 13 and group 15 extrinsic dopants were substituted onto the framework, were also evaluated.[116, 117] It was found that traditional p-type and n-type dopants such as Ga, and P and As, respectively, could be substituted into $CaGe_2$ during synthesis and are retained on the 2D GeH lattice after topotactic deintercalation. Indeed a maximum concentration of 1.0% P, 1.1% As, and 2.3 % Ga could be substituted onto the lattice. However, the simple substitution of group 13 and group 15 atoms does not necessarily lead to p-type and n-type doping. GeH, P:GeH, and As:GeH all remained highly resistive under vacuum. For undoped, 0.5% and 1.0% P-doped GeH the room temperature in-plane and out-of-plane conductivities were observed to be ~$10^{-8}$ and ~$10^{-15}$ $\Omega^{-1}cm^{-1}$ in vacuum. This in-plane conductivity is ~$10^{12}$ greater than that reported for $SiH_{0.5}(OH)_{0.5}$. The in-plane conductivity values for P- and As-doped GeH increase an additional 3 orders of magnitude upon exposure to $H_2O$ containing atmospheres, which suggest that $H_2O$ is necessary to activate the n-type dopant. If P and As are not terminated with –H, these n-type "dopants" are isoelectronic to a "Ge-H" moiety, and thus will not provide an additional electron carrier. In contrast, the introduction of Ga into the framework can decrease the in-plane sheet resistance in vacuum, by over 4 orders of magnitude, with minimal hysteretic behavior. If Ga is not terminated with –H, the empty $p_z$ orbital could provide a hole carrier. While doping appreciably increases the conductivity, these values remain many orders of magnitude lower than other semiconducting 2D materials. This suggests that deep-level defects or other types of structural disorder are limiting the conductivity. Further methods to reduce the disorder in these materials are required before more complex semiconducting devices can be explored. This is fundamentally challenging due to the metastable nature of these materials, which prevents reducing defect concentrations via thermal annealing.

There have been a couple of studies building protoype optoelectronic devices of these materials. For instance, photoconductors have been constructed using $SiH_{0.5}(OH)_{0.5}$, GeH, and $Sn_xGe_{1-x}H_x(OH)_{1-x}$.[59, 117] **Fig. 29** shows a prototypical photoconducting device. The above band gap photoexcitation of carriers in these semiconductors will lead to an increase in current. The wavelength dependence of photoexcitation typically matches the absorption spectrum of the material, and can be tuned by both ligand termination and the main group framework. Additionally, the use of $SiH_{0.5}(OH)_{0.5}$ as an active material in a light-emitting diode was explored.[118] A device consisting of the epitaxial growth of 500 nm thick $SiH_{0.5}(OH)_{0.5}$ on p-type Si(110) showed diode-type rectification in its current vs. voltage measurements. However, electroluminescence, if present, was below the limits of detection.

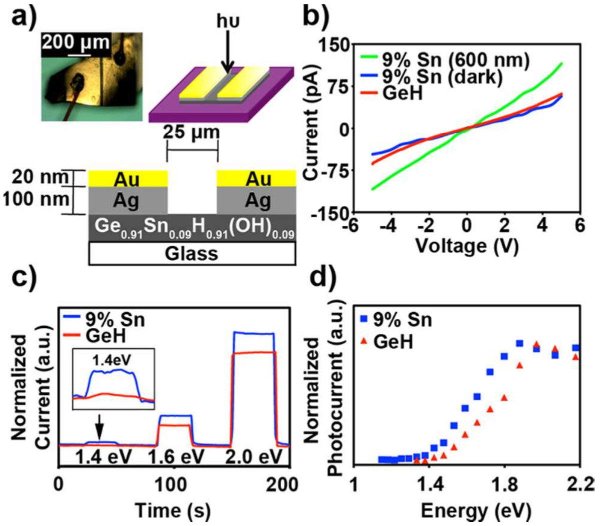

**Fig. 29.** a) Image (Left) of the actual photodetector based on $Ge_{0.91}Sn_{0.09}H_{0.91}(OH)_{0.09}$ and schematic (right) illustration and dimensions of the debvice (not drawn to scale). b) Typical I-V plot of the $Ge_{0.91}Sn_{0.09}H_{0.91}(OH)_{0.09}$ photodectetor in the dark and at 600 nm illumination. c) Photocurrent response at selected illumination wavelengths and d) wavelength-dependent normalized photocurrent for the $Ge_{0.91}Sn_{0.09}H_{0.91}(OH)_{0.09}$ photodectector compared to GeH at a 3 V bias voltage. Reproduced from ref. [59] with permission from Chemistry of Materials, copyright 2014.

### H.2 Quantum spin Hall predictions in 2D SnR

One of the most exciting, and if it could be realized, most impactful phenomenon predicted in these graphane analogues is the emergence of a quantum spin Hall (QSH) insulator state at room temperature in the functionalized Sn graphane analogues.[101] In a quantum spin Hall insulator, the intrinsic spin orbit coupling provides a strong enough magnetic field to make the bulk of the material an insulator with gapless spin-up and spin down conducting edge states that are protected against back scattering.[119, 120] These edge channels are restrained to two possible spin states and are perfect, dissipationless conductors, that are highly resistant to defect and impurity scattering (**Fig. 30a**). Achieving dissipationless conductivity has been a long-standing challenge in materials research since the initial discovery of superconductivity.

Because the spin orbit splitting in the Sn-graphane materials is ~0.3 eV, these dissipationless channels can occur above room temperature. The existence of a 2D topological state depends in these materials on the identity of the surface functionalization group (**Fig. 30b**). SnH is a trivial insulator and does not exhibit a QSH effect. The CBM is comprised of Sn—H σ* states that are of predominantly Sn 5s character, while the two VBM at Gamma are comprised of in-plane Sn—Sn bonding between $5p_x$ and $5p_y$ orbitals, that are split on account of spin-orbit coupling (**Fig. 30c**). Replacing H-termination with a more electron-withdrawing substituent (i.e. a halogen, or –OH) causes the lattice to expand, and raises the energy of the VBM levels. This causes the Sn 5s σ* levels to become lower in energy than the $p_x$ and $p_y$ states, leading to partial $p_x$ and $p_y$ character in both the CBM and the VBM (**Fig. 30d**). Therefore, these materials become QSH insulators.

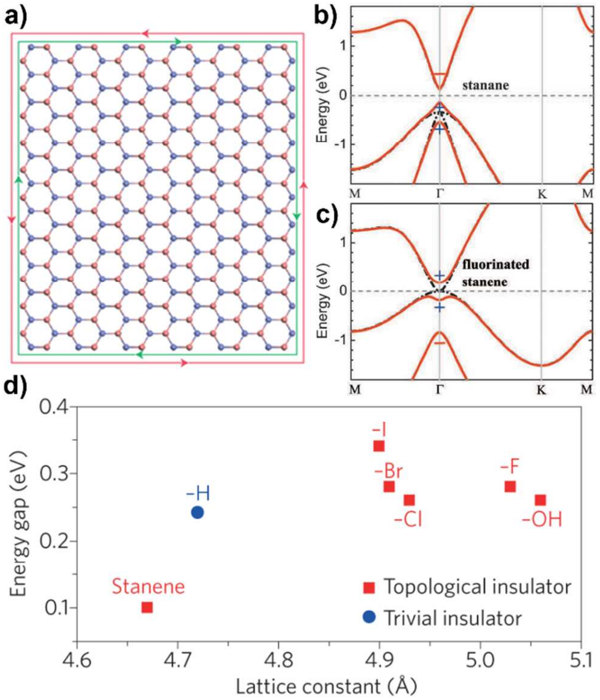

**Fig. 30.** a) Top view of 2D-halogen-terminated stanane in a QSH state bearing helical currents at the edges. Upper and lower positions in the 2D—Sn framework are denoted by red and blue atoms, respectively. Band structures for b) stanane without (black dash-dotted lines) and with (red solid lines) spin-orbital coupling and c) fluorinated stanene. d) Energy gap as a function of the lattice constant induced by the covalent functionalization of stanene. Reproduced from ref. [121] with permission from Nature Materials, copyright 2017. Reproduced from ref. [101] with permission from Physical Review Letters, copyright 2013.

Many other graphane materials have been predicted to become QSH insulators when the band gap is lower in energy than the splitting between the $p_x$ and $p_y$ levels. One such way of achieving a small band gap is via tensile strain. For instance, $GeCH_3$ is also predicted to become a QSH insulator when tensile strain exceeds 12%.[122] While these predictions are scientifically interesting, it remains extremely challenging to experimentally access tensile strains that are larger than 1% in these and most other 2D materials. Most of these predictions refer to the fact that graphene can accommodate large strain values of up to 12% before fracturing.[123] However, graphite is unique in that the C=C lengths are ~1.42 Å while C-C single bonds are ~1.54 Å (which is an 8% difference). However, an 8% increase in the 2.54 Å bond length in Ge-Ge would stretch it to 2.74 Å, which is virtually unheard of in any known material.

### H.3 Batteries

Silicon and germanium nanomaterials have generated considerable interest as Li ion battery anodes due to the large capacity in Li-Si and Li-Ge alloys.[124-127] $Li_{15}Si_4$ exhibits a high theoretical capacity of 3570 mAh $g^{-1}$ at room temperature. $Li_{15}Ge_4$ has a theoretical capacity of 1384 mAh $g^{-1}$, and a high lithium diffusivity. However, these materials have significant shortcomings as their capacity fades after a few cycles and they have low coulombic efficiencies. One of the factors that limits cyclability are the volume changes that occur upon multiple-charging and discharging cycles. Recently, silicane and germanane materials have been explored for use as anode materials. It has been reported that their 2D nature allows for a higher capacitance and smaller change in volume than silicon or germanium powders.

SiH has been evaluated for use as anodes in both Li-ion batteries and more recently in $BF_4^-$ anion batteries. First, SiH/graphite composites can indeed be utilized as anodes for Li-ion batteries, and their performance was compared to polycrystalline silicon. During the first cycle, SiH anodes become amorphous upon lithiation, whereas a silicon powder anode will transform into crystalline $Li_{15}Si_4$. After 10 lithiation/delithiation cycles the layered polysilane anodes remain amorphous whereas polycrystalline Si will slowly amorphize.[128] The volume increase upon lithiation is smaller for SiH, since the density of Si in the 2D materials is much smaller. It was found that both SiH and silicon powder anodes lose half of their capacity after 10 cycles.[129] Higher cyclability was obtained by precoating the layered polysilane with carbon either via pulsed laser deposition, or via the graphitization of SiH/sucrose composites. While this work does indeed show that layered polysilane can indeed be used as a Li-ion anode, and it exhibits smaller changes in volume than silicon powders, achieving long-term cyclability still requires future research efforts.

A reversible anion battery in which $BF_4^-$ is intercalated into and deintercalated from (2-dimethylamino)ethanol-terminated silicane was demonstrated.[130] Using a graphite cathode, 0.2 eq. of $BF_4^-$ can be reversibly intercalated into $[SiH_{0.8}(O(CH_2)_2NH(CH_3)_2)_{0.2}][BF_4]_{0.2}$, at a potential difference of 1.8 V and an initial capacity of 80 mAh $g^{-1}$. The first charge and discharge cycle lead to an irreversible capacity loss of ~35% which subsequently faded by ~2% per cycle. Despite having a low capacity, this anion battery could be cycled 100x at 40 $^oC$ while maintaining a capacity above 50 mAh $g^{-1}$. Furthermore these anion batteries showed excellent performance at very low temperatures and, in contrast to Li-ion batteries, could even be charged and discharged at -30 $^oC$.

Serino *et al.* explored the use of germanane as an anode material for Li-ion batteries. The authors were able to prepare batteries that had a reversible Li-ion capacity of 1108 mAh $g^{-1}$ when cycled between 0.1 and 2 V vs. $Li/Li^+$.[131] These anodes come close to the theoretical maximum of energy storage, maintain their capacity after 100 charge/discharge cycles, and operate effectively with fast cycling rates. Similar to SiH, after the first charge and discharge cycle GeH was observed to transform into amorphous Ge.

### H.4 Photocatalysis

Since SiH and GeH are semiconductors with tunable band gaps, recent work has explored their use as photocatalysis. Liu *et al.* reported that GeH can photocatalyze both the decomposition of conjugated organic molecules and the hydrogen evolution reaction of water splitting using broadband visible wavelengths >420 nm.[132] The authors showed that Rhodamine B can be degraded upon GeH photoexcitation, with an estimated rate constant of 0.197 $min^{-1}$ assuming first order kinetics. This was 6x faster than an N-doped $TiO_2$ control photocatalyst. Second, GeH decorated with 1 wt% Pt nanoparticles in $CH_3OH/H_2O$ was able to generate $H_2$ at a rate of 22 μmol $h^{-1}$ $g^{-1}$. The decoration of Pt nanoparticles was not necessary for $H_2$ generation but improved the rate by a factor of 3x. Minimal loss of activity was observed in either the photodegradation or hydrogen evolution experiments, highlighting the water stability of GeH. Future studies quantifying the photonic efficiencies and quantum yields in these heterogeneous photocatalysts efficiency will enable more systematic explorations of the role of ligand functionalization on performance.

## Conclusions

In this review, we have summarized and highlighted recent advances in the surface functionalization chemistry of 2D materials, and in particular the group 14 graphane analogues. This family of 2D materials is an ideal system for understanding the influence of ligand design on properties and stability, since every atom on the framework requires a surface bound ligand. The ligand density that can be achieved on these group 14 graphane materials is effectively a monolayer, and is many times larger than what has been shown for other 2D materials including graphene, transition metal dichalcogenides, and phosphorene.

Although the group 14 graphane analogues can trace their history back to the 1860's, these materials remain much less well studied than the transition metal dichalcogenides and graphene. While numerous methods towards functionalization of Si/Ge(111) surfaces have been previously established, only recently have researchers started to investigate these with graphane analogues. Several routes have been reported including the direct topotactic transformation of precursor Zintl phases, as well as the substitution of H-termination with other ligands. It has become clear that the reactivity of these graphane analogues are strikingly different than Si/Ge(111) surfaces despite their structural similarity. Additionally, these frameworks are more prone to amorphization, either thermally, or via free-radical based functionalization mechanisms. Ultimately, our understanding of these materials and their functionalization remains in its infancy. The quantitative and systematic comparisons of the different functionalization methodologies and their mechanistic pathways will be extremely impactful and are of paramount importance in the future.

The covalent functionalization of 2D materials is a remarkable new regime in materials research. In contrast to nanoparticles and solid-state materials, where the outer surface represents only a small fraction of the whole material, the electronic structure and thermal stability of these single-atom thick graphane ligands are dictated by the identity of the terminal ligand. Initial work has shown that for a given framework, the band gaps can be rationally tailored by at least >15%, and that more electron withdrawing and larger ligands will lead to smaller band gaps and expanded frameworks. Still, there is a limit to the size of the ligand that can be grafted onto the surface, and ligands that are too sterically bulky will result in partial termination. Furthermore, the thermal stability has been shown to improve with different ligands and in some cases increase by >100 $^{o}$C. While these materials have begun to be exploited in applications including field effect transistors, photodetectors, batteries, and photocatalysts, the ability to tailor the surface chemistry gives these materials great potential in chemical and biochemical sensing and membrane technologies. Furthermore, the realization of the exotic physical phenomena that can be accessed via chemical control of the band structure, such as robust, dissipationless transport at room temperature, would be revolutionary. Creating such systems will require the close integration between theory and experimental researchers. To conclude, these atomic-scale materials merge the disparate nature of organic and solid-state chemistry, giving these systems a bright and promising future.

## Conflicts of interest

There are no conflicts to declare.

## Acknowledgements

Primary funding for this research was provided by NSF EFRI-1433467. We acknowledge partial support from the Center for Emergent Materials: an NSF MRSEC under award number DMR-1420451. J.E.G acknowledges the Camille and Henry Dreyfus Foundation for partial support.

## References

1. K. S. Novoselov, A. K. Geim, S. Morozov, D. Jiang, M. Katsnelson, I. Grigorieva, S. Dubonos and A. Firsov, *Nature (London, U. K.)*, 2005, **438**, 197.
2. K. F. Mak, C. Lee, J. Hone, J. Shan and T. F. Heinz, *Phys. Rev. Lett.*, 2010, **105**, 136805.
3. Q. H. Wang, Z. Jin, K. K. Kim, A. J. Hilmer, G. L. Paulus, C.-J. Shih, M.-H. Ham, J. D. Sanchez-Yamagishi, K. Watanabe and T. Taniguchi, *Nat. Chem.*, 2012, **4**, 724.
4. B. Huang, G. Clark, E. Navarro-Moratalla, D. R. Klein, R. Cheng, K. L. Seyler, D. Zhong, E. Schmidgall, M. A. McGuire and D. H. Cobden, *Nature (London, U. K.)*, 2017, **546**, 270.
5. J. H. Seol, I. Jo, A. L. Moore, L. Lindsay, Z. H. Aitken, M. T. Pettes, X. Li, Z. Yao, R. Huang and D. Broido, *Science (Washington, DC, U. S.)*, 2010, **328**, 213-216.
6. S. Z. Butler, S. M. Hollen, L. Cao, Y. Cui, J. A. Gupta, H. R. Gutiérrez, T. F. Heinz, S. S. Hong, J. Huang and A. F. Ismach, *ACS Nano*, 2013, **7**, 2898-2926.
7. J. M. Buriak, *Chem. Rev.*, 2002, **102**, 1271-1308.
8. S. F. Bent, *Surf. Sci.*, 2002, **500**, 879-903.
9. L. J. Webb and N. S. Lewis, *J. Phys. Chem. B*, 2003, **107**, 5404-5412.
10. G. W. Cullen, J. A. Amick and D. Gerlich, *J. Electrochem. Soc.*, 1962, **109**, 124-127.
11. R. L. Cicero, M. R. Linford and C. E. Chidsey, *Langmuir*, 2000, **16**, 5688-5695.
12. L. A. Huck and J. M. Buriak, *Langmuir*, 2012, **28**, 16285-16293.
13. K. Choi and J. M. Buriak, *Langmuir*, 2000, **16**, 7737-7741.
14. E. G. Robins, M. P. Stewart and J. M. Buriak, *Chem. Commun. (Cambridge, U. K.)*, 1999, 2479-2480.
15. P. Allongue, C. H. de Villeneuve, G. Cherouvrier, R. Cortes and M.-C. Bernard, *J. Electroanal. Chem.*, 2003, **550**, 161-174.
16. F. Tian, D. F. Taber and A. V. Teplyakov, *J. Am. Chem. Soc.*, 2011, **133**, 20769-20777.
17. P. Ardalan, C. B. Musgrave and S. F. Bent, *Langmuir*, 2009, **25**, 2013-2025.
18. H. Yu, L. J. Webb, J. R. Heath and N. S. Lewis, *Appl. Phys. Lett.*, 2006, **88**, 252111.
19. E. J. Nemanick, P. T. Hurley, B. S. Brunschwig and N. S. Lewis, *J. Phys. Chem. B*, 2006, **110**, 14800-14808.
20. L. E. O'Leary, E. Johansson, B. S. Brunschwig and N. S. Lewis, *J. Phys. Chem. B*, 2010, **114**, 14298-14302.
21. F. Wöhler, *Justus Liebigs Ann. Chem.*, 1863, **127**, 257-274.
22. H. Kautsky, *Z. Anorg. Allg. Chem.*, 1921, **117**, 209-242.
23. H. Kautsky and G. Herzberg, *Z. Anorg. Allg. Chem.*, 1924, **139**, 135-160.
24. H. Pfleger, 1956.
25. A. Weiss, G. Beil and H. Meyer, *Journal*, 1980, **35**, 25.
26. G. Schott, *Z. Chem. (Stuttgart, Ger.)*, 1962, **2**, 194-200.
27. J. R. Dahn, B. M. Way, E. Fuller and J. S. Tse, *Phys. Rev. B*, 1993, **48**, 17872-17877.
28. J. He, Z.-H. Lu, S. A. Mitchell and D. D. Wayner, *J. Am. Chem. Soc.*, 1998, **120**, 2660-2661.
29. J. He, J. Tse, D. Klug and K. Preston, *J. Mater. Chem.*, 1998, **8**, 705-710.
30. N. T. Plymale, Y.-G. Kim, M. P. Soriaga, B. S. Brunschwig and N. S. Lewis, *J. Phys. Chem. C*, 2015, **119**, 19847-19862.
31. N. T. Plymale, M. Dasog, B. S. Brunschwig and N. S. Lewis, *J. Phys. Chem. C*, 2017, **121**, 4270-4282.
32. K. E. Plass, X. Liu, B. S. Brunschwig and N. S. Lewis, *Chem. Mater.*, 2008, **20**, 2228-2233.

33. L. E. O'Leary, N. C. Strandwitz, C. W. Roske, S. Pyo, B. S. Brunschwig and N. S. Lewis, *J. Phys. Chem. Lett.*, 2015, **6**, 722-726.
34. A. Bansal, X. Li, S. I. Yi, W. Weinberg and N. S. Lewis, *J. Phys. Chem. B*, 2001, **105**, 10266-10277.
35. M. R. Linford, P. Fenter, P. M. Eisenberger and C. E. Chidsey, *J. Am. Chem. Soc.*, 1995, **117**, 3145-3155.
36. C. Miramond and D. Vuillaume, *J. Appl. Phys.*, 2004, **96**, 1529-1536.
37. F. Gao and A. V. Teplyakov, *J. Phys. Chem. C*, 2016, **120**, 5539-5548.
38. B. Eves and G. Lopinski, *Surf. Sci.*, 2005, **579**, 89-96.
39. N. T. Plymale, A. A. Ramachandran, A. Lim, B. S. Brunschwig and N. S. Lewis, *J. Phys. Chem. C*, 2016, **120**, 14157-14169.
40. C. J. Barrelet, D. B. Robinson, J. Cheng, T. P. Hunt, C. F. Quate and C. E. Chidsey, *Langmuir*, 2001, **17**, 3460-3465.
41. P. Allongue, C. H. De Villeneuve, J. Pinson, F. Ozanam, J. Chazalviel and X. Wallart, *Electrochim. Acta*, 1998, **43**, 2791-2798.
42. C. H. de Villeneuve, J. Pinson, M. C. Bernard and P. Allongue, *J. Phys. Chem. B*, 1997, **101**, 2415-2420.
43. T. P. Chopra, R. C. Longo, K. Cho, M. D. Halls, P. Thissen and Y. J. Chabal, *Chem. Mater.*, 2015, **27**, 6268-6281.
44. D. Knapp, B. S. Brunschwig and N. S. Lewis, *J. Phys. Chem. C*, 2011, **115**, 16389-16397.
45. D. Knapp, B. S. Brunschwig and N. S. Lewis, *J. Phys. Chem. C*, 2010, **114**, 12300-12307.
46. H. Okamoto, Y. Kumai, Y. Sugiyama, T. Mitsuoka, K. Nakanishi, T. Ohta, H. Nozaki, S. Yamaguchi, S. Shirai and H. Nakano, *J. Am. Chem. Soc.*, 2010, **132**, 2710-2718.
47. S. Yamanaka, H. Matsu-ura and M. Ishikawa, *Mater. Res. Bull.*, 1996, **31**, 307-316.
48. T. Helbich, A. Lyuleeva, P. Marx, L. M. Scherf, T. K. Purkait, T. F. Fässler, P. Lugli, J. G. C. Veinot and B. Rieger, *Adv. Func. Mater.*, 2017, **27**, 1606764-n/a.
49. E. Bonitz, *Chem. Ber.*, 1961, **94**, 220-225.
50. G. Vogg, M. S. Brandt and M. Stutzmann, *Adv. Mater.*, 2000, **12**, 1278-1281.
51. E. Bianco, S. Butler, S. Jiang, O. D. Restrepo, W. Windl and J. E. Goldberger, *ACS Nano*, 2013, **7**, 4414-4421.
52. N. D. Cultrara, Y. Wang, M. Q. Arguilla, M. R. Scudder, S. Jiang, W. Windl, S. Bobev and J. E. Goldberger, *Chem. Mater.*, 2018, **30**, 1335-1343.
53. S. Jiang, E. Bianco and J. E. Goldberger, *J. Mater. Chem. C*, 2014, **2**, 3185-3188.
54. X. Liang, Y.-G. Kim, D. K. Gebergziabiher and J. L. Stickney, *Langmuir*, 2010, **26**, 2877-2884.
55. N. N. Bui, M. Ledina, T. J. Reber, J. Jung and J. L. Stickney, *ACS Nano*, 2017, **11**, 9481-9489.
56. M. A. Ledina, N. Bui, X. Liang, Y.-G. Kim, J. Jung, B. Perdue, C. Tsang, J. Drnec, F. Carlà, M. P. Soriaga, T. J. Reber and J. L. Stickney, *J. Electrochem. Soc.*, 2017, **164**, D469-D477.
57. S.-J. Kim and F. Fässler Thomas, *Journal*, 2008, **223**, 325.
58. M. Q. Arguilla, N. D. Cultrara, M. R. Scudder, S. Jiang, R. D. Ross and J. E. Goldberger, *J. Mater. Chem. C*, 2017, **5**, 11259-11266.
59. M. Q. Arguilla, S. Jiang, B. Chitara and J. E. Goldberger, *Chem. Mater.*, 2014, **26**, 6941-6946.
60. S. Jiang, M. Q. Arguilla, N. D. Cultrara and J. E. Goldberger, *Chem. Mater.*, 2016, **28**, 4735-4740.
61. S. Jiang, K. Krymowski, T. Asel, M. Q. Arguilla, N. D. Cultrara, E. Yanchenko, X. Yang, L. J. Brillson, W. Windl and J. E. Goldberger, *Chem. Mater.*, 2016, **28**, 8071-8077.
62. R. Ramachandran, D. Johnson-McDaniel and T. T. Salguero, *Chem. Mater.*, 2016, **28**, 7257-7267.
63. R. Yaokawa, T. Ohsuna, T. Morishita, Y. Hayasaka, M. J. S. Spencer and H. Nakano, *Nat. Commun.*, 2016, **7**, 10657.
64. R. Yaokawa, T. Ohsuna, Y. Hayasaka and H. Nakano, *ChemistrySelect*, 2016, **1**, 5579-5583.
65. H. Nakano, M. Nakano, K. Nakanishi, D. Tanaka, Y. Sugiyama, T. Ikuno, H. Okamoto and T. Ohta, *J. Am. Chem. Soc.*, 2012, **134**, 5452-5455.
66. T. Helbich, A. Lyuleeva, I. Höhlein, P. Marx, L. M. Scherf, J. Kehrle, T. F. Fässler, P. Lugli and B. Rieger, *Chem. - Eur. J.*, 2016, **22**, 6194-6198.
67. H. Yu, T. Helbich, L. M. Scherf, J. Chen, K. Cui, T. F. Fässler, B. Rieger and J. G. C. Veinot, *Chem. Mater.*, 2018, **30**, 2274-2280.
68. H. Okamoto, Y. Sugiyama, K. Nakanishi, T. Ohta, T. Mitsuoka and H. Nakano, *Chem. Mater.*, 2015, **27**, 1292-1298.
69. J. Ohshita, K. Yamamoto, D. Tanaka, M. Nakashima, Y. Kunugi, M. Ohashi and H. Nakano, *J. Phys. Chem. C*, 2016, **120**, 10991-10996.
70. Y. Sugiyama, H. Okamoto, T. Mitsuoka, T. Morikawa, K. Nakanishi, T. Ohta and H. Nakano, *J. Am. Chem. Soc.*, 2010, **132**, 5946-5947.
71. S. Jiang, M. Q. Arguilla, N. D. Cultrara and J. E. Goldberger, *Acc. Chem. Res.*, 2015, **48**, 144-151.
72. M. Pumera and C. H. A. Wong, *Chem. Soc. Rev.*, 2013, **42**, 5987-5995.
73. G. Yang, D. Bao, H. Liu, D. Zhang, N. Wang and H. Li, *J. Inorg. Organomet. Polym. Mater.*, 2017, **27**, 1129-1141.
74. S. Presolski and M. Pumera, *Mater. Today*, 2016, **19**, 140-145.
75. C. R. Ryder, J. D. Wood, S. A. Wells and M. C. Hersam, *ACS nano*, 2016, **10**, 3900-3917.
76. D. C. Elias, R. R. Nair, T. M. G. Mohiuddin, S. V. Morozov, P. Blake, M. P. Halsall, A. C. Ferrari, D. W. Boukhvalov, M. I. Katsnelson, A. K. Geim and K. S. Novoselov, *Science (Washington, DC, U. S.)*, 2009, **323**, 610-613.
77. R. A. Schäfer, J. M. Englert, P. Wehrfritz, W. Bauer, F. Hauke, T. Seyller and A. Hirsch, *Angew. Chem., int. Ed*, 2013, **52**, 754-757.
78. W. Feng, P. Long, Y. Feng and Y. Li, *Adv. Sci. (Weinheim, Ger.)*, 2016, **3**, 1500413-n/a.
79. E. Bekyarova, M. E. Itkis, P. Ramesh, C. Berger, M. Sprinkle, W. A. de Heer and R. C. Haddon, *J. Am. Chem. Soc.*, 2009, **131**, 1336-1337.
80. P. Allongue, M. Delamar, B. Desbat, O. Fagebaume, R. Hitmi, J. Pinson and J.-M. Savéant, *J. Am. Chem. Soc.*, 1997, **119**, 201-207.
81. R. Poe, K. Schnapp, M. J. Young, J. Grayzar and M. S. Platz, *J. Am. Chem. Soc.*, 1992, **114**, 5054-5067.
82. W. T. Borden, N. P. Gritsan, C. M. Hadad, W. L. Karney, C. R. Kemnitz and M. S. Platz, *Acc. Chem. Res.*, 2000, **33**, 765-771.
83. H. He and C. Gao, *Chem. Mater.*, 2010, **22**, 5054-5064.
84. J. Choi, K.-j. Kim, B. Kim, H. Lee and S. Kim, *J. Phys. Chem. C*, 2009, **113**, 9433-9435.
85. P. A. Denis and F. Iribarne, *J. Phys. Chem. C*, 2010, **115**, 195-203.

86. R. Nair and W. Ren, *Small*, 2010, **6**, 2877.
87. J. Robinson, *Nano Lett.*, 2010, **10**, 3001.
88. X. Gao and X. S. Tang, *Carbon*, 2014, **76**, 133-140.
89. K. Samanta, S. Some, Y. Kim, Y. Yoon, M. Min, S. M. Lee, Y. Park and H. Lee, *Chem. Commun. (Cambridge, U. K.)*, 2013, **49**, 8991-8993.
90. W. H. Lee, J. W. Suk, H. Chou, J. Lee, Y. Hao, Y. Wu, R. Piner, D. Akinwande, K. S. Kim and R. S. Ruoff, *Nano Lett.*, 2012, **12**, 2374-2378.
91. H. Chang, J. Cheng, X. Liu, J. Gao, M. Li, J. Li, X. Tao, F. Ding and Z. Zheng, *Chem. - Eur. J.*, 2011, **17**, 8896-8903.
92. H. Ismaili, D. Geng, A. X. Sun, T. T. Kantzas and M. S. Workentin, *Langmuir*, 2011, **27**, 13261-13268.
93. T. Sainsbury, M. Passarelli, M. Naftaly, S. Gnaniah, S. J. Spencer and A. J. Pollard, *ACS Appl. Mater. Interfaces*, 2016, **8**, 4870-4877.
94. D. Voiry, A. Goswami, R. Kappera, C. d. C. C. e. Silva, D. Kaplan, T. Fujita, M. Chen, T. Asefa and M. Chhowalla, *Nat. Chem.*, 2014, **7**, 45.
95. K. C. Knirsch, N. C. Berner, H. C. Nerl, C. S. Cucinotta, Z. Gholamvand, N. McEvoy, Z. Wang, I. Abramovic, P. Vecera, M. Halik, S. Sanvito, G. S. Duesberg, V. Nicolosi, F. Hauke, A. Hirsch, J. N. Coleman and C. Backes, *ACS Nano*, 2015, **9**, 6018-6030.
96. S. S. Chou, M. De, J. Kim, S. Byun, C. Dykstra, J. Yu, J. Huang and V. P. Dravid, *J. Am. Chem. Soc.*, 2013, **135**, 4584-4587.
97. L. Zhou, B. He, Y. Yang and Y. He, *RSC Adv.*, 2014, **4**, 32570-32578.
98. C. R. Ryder, J. D. Wood, S. A. Wells, Y. Yang, D. Jariwala, T. J. Marks, G. C. Schatz and M. C. Hersam, *Nat. Chem.*, 2016, **8**, 597.
99. O. D. Restrepo, R. Mishra, J. E. Goldberger and W. Windl, *J. Appl. Phys.*, 2014, **115**, 033711.
100. W. Amamou, P. M. Odenthal, E. J. Bushong, D. J. O'Hara, Y. K. Luo, J. Van Baren, I. Pinchuk, Y. Wu, A. S. Ahmed and J. Katoch, *2D Mater.*, 2015, **2**, 035012.
101. Y. Xu, B. Yan, H.-J. Zhang, J. Wang, G. Xu, P. Tang, W. Duan and S.-C. Zhang, *Phys. Rev. Lett.*, 2013, **111**, 136804.
102. C. G. Van de Walle and J. E. Northrup, *Phys. Rev. Lett.*, 1993, **70**, 1116.
103. L. Brus, *J. Phys. Chem.*, 1994, **98**, 3575-3581.
104. O. D. Restrepo, K. E. Krymowski, J. Goldberger and W. Windl, *New J. Phys.*, 2014, **16**, 105009.
105. G. Vogg, A.-P. Meyer, C. Miesner, M. Brandt and M. Stutzmann, *Appl. Phys. Lett.*, 2001, **78**, 3956-3958.
106. G. Vogg, L. J.-P. Meyer, C. Miesner, M. S. Brandt and M. Stutzmann, *Monatsh. Chem.*, 2001, **132**, 1125-1135.
107. C. Canali, C. Jacoboni, F. Nava, G. Ottaviani and A. Alberigi-Quaranta, *Phys. Rev. B*, 1975, **12**, 2265.
108. C. Jacoboni, C. Canali, G. Ottaviani and A. A. Quaranta, *Solid-State Electron.*, 1977, **20**, 77-89.
109. C. Jacoboni, F. Nava, C. Canali and G. Ottaviani, *Phys. Rev. B*, 1981, **24**, 1014.
110. G. Ottaviani, C. Canali, F. Nava and J. Mayer, *J. Appl. Phys.*, 1973, **44**, 2917-2918.
111. X. Pi, Z. Ni, Y. Liu, Z. Ruan, M. Xu and D. Yang, *Phys. Chem. Chem. Phys.*, 2015, **17**, 4146-4151.
112. A. C. Ferrari and J. Robertson, *Phys. Rev. B*, 2000, **61**, 14095.
113. G. Coloyan, N. D. Cultrara, A. Katre, J. Carrete, M. Heine, E. Ou, J. Kim, S. Jiang, L. Lindsay and N. Mingo, *Appl. Phys. Lett.*, 2016, **109**, 131907.
114. M. Brandt, T. Puchert and M. Stutzmann, *Solid State Commun.*, 1997, **102**, 365-368.
115. B. Madhushankar, A. Kaverzin, T. Giousis, G. Potsi, D. Gournis, P. Rudolf, G. Blake, C. van der Wal and B. van Wees, *2D Mater.*, 2017, **4**, 021009.
116. N. D. Cultrara, M. Q. Arguilla, S. Jiang, C. Sun, M. R. Scudder, R. D. Ross and J. E. Goldberger, *Beilstein J. Nanotechnol.*, 2017, **8**, 1642-1648.
117. J. R. Young, B. Chitara, N. D. Cultrara, M. Q. Arguilla, S. Jiang, F. Fan, E. Johnston-Halperin and J. E. Goldberger, *J. Phys.: Condens. Matter*, 2016, **28**, 034001.
118. G. Vogg, N. Zamanzadeh-Hanebuth, M. S. Brandt, M. Stutzmann and M. Albrecht, *Monatsh. Chem.*, 1999, **130**, 79-87.
119. C. L. Kane and E. J. Mele, *Phys. Rev. Lett.*, 2005, **95**, 146802.
120. M. König, S. Wiedmann, C. Brüne, A. Roth, H. Buhmann, L. W. Molenkamp, X.-L. Qi and S.-C. Zhang, *Science (Washington, DC, U. S.)*, 2007, **318**, 766-770.
121. A. Molle, J. Goldberger, M. Houssa, Y. Xu, S.-C. Zhang and D. Akinwande, *Nat. Mater.*, 2017, **16**, 163.
122. Y. Ma, Y. Dai, W. Wei, B. Huang and M.-H. Whangbo, *Sci. Rep.*, 2014, **4**, 7297.
123. C. Lee, X. Wei, J. W. Kysar and J. Hone, *Science (Washington, DC, U. S.)*, 2008, **321**, 385-388.
124. M. T. McDowell, S. W. Lee, W. D. Nix and Y. Cui, *Adv. Mater.*, 2013, **25**, 4966-4985.
125. C. K. Chan, H. Peng, G. Liu, K. McIlwrath, X. F. Zhang, R. A. Huggins and Y. Cui, *Nat. Nanotechnol.*, 2008, **3**, 31.
126. T. Kennedy, E. Mullane, H. Geaney, M. Osiak, C. O'Dwyer and K. M. Ryan, *Nano Lett.*, 2014, **14**, 716-723.
127. J. Graetz, C. Ahn, R. Yazami and B. Fultz, *J. Electrochem. Soc.*, 2004, **151**, A698-A702.
128. Y. Kumai, S. Shirai, E. Sudo, J. Seki, H. Okamoto, Y. Sugiyama and H. Nakano, *J. Power Sources*, 2011, **196**, 1503-1507.
129. Y. Kumai, S. Shirai, H. Okamoto, Y. Sugiyama and H. Nakano, *IOP Conf. Series: Matet. Sci. Eng.*, 2011, **18**, 122005.
130. H. Nakano, Y. Sugiyama, T. Morishita, M. J. S. Spencer, I. K. Snook, Y. Kumai and H. Okamoto, *J. Mater. Chem. A*, 2014, **2**, 7588-7592.
131. A. C. Serino, J. S. Ko, M. T. Yeung, J. J. Schwartz, C. B. Kang, S. H. Tolbert, R. B. Kaner, B. S. Dunn and P. S. Weiss, *ACS Nano*, 2017, **11**, 7995-8001.
132. Z. Liu, Z. Lou, Z. Li, G. Wang, Z. Wang, Y. Liu, B. Huang, S. Xia, X. Qin and X. Zhang, *Chem. Commun. (Cambridge, U. K.)*, 2014, **50**, 11046-11048.

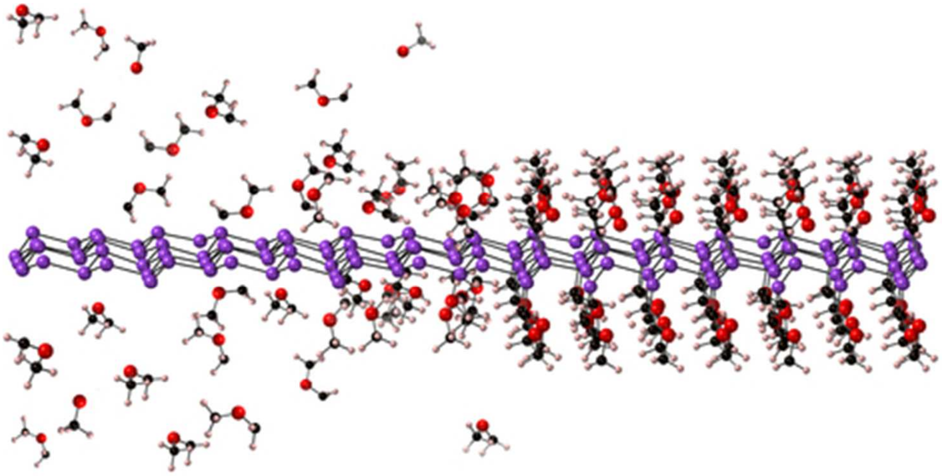

39x19mm (300 x 300 DPI)